On the use of Glimm-like schemes for transport equations on multi-dimensional domain

Olivier Hurisse

On the use of Glimm-like schemes for transport equations on multi-dimensional domain.

Olivier Hurisse

Contents

1 Introduction

The numerical simulation of front propagation has been widely investigated in the literature and a large range of methods have been proposed. In the present work, and in this introduction, we cannot pretend to make a complete overview of this research area. Proposing an exhaustive review is out of the scope of the present paper. An helpful review on the subject of sharpening methods and front tracking has recently been proposed, see [9, 19]. We restrict ourselves here to methods that are based on classical finite volumes approaches, including: high-order schemes, anti-diffusion methods or the Glimm's method originally issued from [13]. Obviously, several other kinds of methods have been proposed in the literature. We intend to present here a method based on the classical finite volumes approach and relying on Glimm's ideas. Sharpening methods [9] concerns the general problem of the advection of a scalar quantity by a velocity field when associated with a linearly degenerate field. In the present work we are only interested by a sub-class of this class of problems: the scalar quantity is supposed to take only two distinct values. So that it can be assimilated to the advection of an indicator function within a velocity field (and associated with a linearly degenerate field). This could thus be seen as a front tracking situation.

An easy way of modeling such front propagation problems is indeed based on the advection equation. For that purpose, a scalar quantity ϕ is defined and takes two different values, say 0 and 1 for instance, on each side of a front. Considering the one-dimensional advection problem of the quantity ϕ with the velocity field $\mathcal{U}$, the following model can classically be considered:

$$\left\{ \begin{array}{l} \partial_t \left(\phi(t,x)\right) + \mathcal{U}(t,x)\partial_x \left(\phi(t,x)\right) = 0, \\ \phi(t=0,x) \in \{0,1\}. \end{array} \right. \tag{1}$$

Provided that $\mathcal{U}$ is a smooth velocity field and that it does not depend on ϕ, the front propagation will be associated with a contact wave (i.e. a linearly degenerate field). An important point to be quoted for the solutions of system (1) is that: at any time t and at any point x, the scalar quantity $\phi(t,x)$ lies in $\{0,1\}$. Providing numerical methods based on finite volumes and that are able to compute satisfactory approximated solutions of system (1) is a tricky task. Indeed, the major drawback of these methods is that the approximations of the scalar quantity ϕ take values that can be different from 0 or 1. In the following paragraph, we propose a brief insight in some classical sharpening methods, whose aim in this situation is to limit the size of the domain where $\phi(t,x) \notin \{0,1\}$ while keeping track of the location of the front.

A wide range of high-order methods [21] and anti-diffusion schemes have been developed during the last decades [9]. They provide accurate approximations for scalar advection which is a more general framework than the advection of an indicator function by the mean of system (1). For our specific problem, the main drawback of these methods is that they tend to produce numerical values that do not remain in $\{0,1\}$. Some anti-diffusion schemes succeed in keeping the discrete approximations of the solution of (1) in $\{0,1\}$ when considering the one-dimensional setting, but their extension to the framework of unstructured multi-dimensional meshes may become complex. This is for instance the case for the Glimm's method derived from [13] and studied in details in [3, 4, 14, 5]. In order to keep the approximated solutions in $\{0,1\}$, this method seems very appealing. For classical finite volumes methods, the time-marching algorithm updates the value in a cell by the mean of a formula "mixing" the values of the neighboring cells. The appearance of discrete values different from 0 and 1 arises from this update formula. The idea issued from the work of Glimm, and applied to our specific case, is that: if at the beginning of the time-step the discrete values are in $\{0,1\}$ for all the cells, then updating the value of a cell by using one value taken among the neighboring cells cannot create new values. Glimm's proposition consists in choosing this updated value in a random manner. Obviously the Glimm's method applies to more complex problems [2, 6, 1] and it can even be used in the multi-dimensional framework when considering structured meshes and an ADI fractional step approach [16, 17]. Nevertheless, it is known that the original Glimm's method cannot be extended to multidimensional unstructured meshes.

Some works have been carried out in order to use the Glimm's idea on complex problems, see among other [2, 6, 1]. Concerning the more simple problem of transport of an indicator function assessed in the present work, the reference [7] has to be highlighted. In this paper, the authors present a probabilistic analysis of the classical finite-volumes Upwind scheme. The approximated solutions of the latter are built as the expectation of a stochastic process, where the characteristics are stochastic and follow a Markov chain. It arises from this analysis that the effective order of $1/2$ of the Upwind scheme can be associated to the fluctuations of the stochastic characteristics around the average characteristic, and to the expectation operator applied to recover the Upwind scheme. The basic idea of the scheme proposed here is thus that, following Glimm's idea, selecting only one sample of this stochastic process avoid to apply an expectation operator. Doing so, we could expect to get an effective convergence rate higher than $1/2$ and a better accuracy for the approximated solutions. In the following, such a strategy is proposed on the basis of a fractional step approach. The first step is performed using a classical finite-volumes scheme and it can be seen as a way to compute the average characteristics for the transport equation. This first step can be performed with a lot of different schemes, even if we have mainly used the Upwind scheme. Then, one sample of the characteristic is selected during the second step on the basis of a random choice. This second step is nicknamed GRU (for Glimm Random Update) in the following. It can thus be seen as the random choice of one sample of an underlying stochastic process for the characteristics, whose transition probabilities are obtained by the scheme used for the first step.

The method proposed here has several strong advantages. First of all, the approximated values remain in $\{0,1\}$ so that the approximated solutions for ϕ are always indicator functions. An important advantage is that the method is extremely simple to implement and, since the GRU step is performed through a fractional step, it can be used with a lot of different schemes. Moreover, the random update is performed cell-wise which implies that its is well-suited for multi-processor computations without any additional development. At last, the most remarkable point is that it extends very naturally to the multi-dimensional framework with unstructured meshes. It should be highlighted once more that the implementation for multi-dimensional unstructured meshes does not require much work than for the one-dimensional framework.

The outline of the paper is the following. The basic idea of the scheme and some properties are presented in section 2 and in appendix (6.1). One-dimensional test cases are investigated in order to compare the original Glimm's method and the GRU method on the basis of the analytical solution given in appendix. Appendix 6.4 provides additional results for the GRU step when considering a non-conservative framework. In section 3, the GRU step is used to treat the scalar advection for a simple two-phase flow model based on the Euler system of equations. At last, some basic multi-dimensional test cases on structured and unstructured meshes are reported in section 4. These test cases involve the propagation of a planar front or the rotation of different shapes. Section 4 provides an illustration of the robustness of the method proposed here. For all the test cases involved in this paper, convergence studies have been performed and comparisons with classical finite-volumes schemes are provided.

2   A Glimm-like scheme for a one-dimensional advection problem in conservative form

We intend here to perform some tests on the advection of a scalar in the framework of the compressible flows. For that purpose, we consider in this section the following one-dimensional system in conservative form:

$$\begin{cases} \partial_t (\rho) + \partial_x (\rho U) = 0, \\ \partial_t (\rho\phi) + \partial_x (\rho U\phi) = 0, \end{cases} \tag{2}$$

where the initial conditions for the scalar quantity $\phi(t,x)$ are: $\forall x, \ \phi(t=0,x) \in \{0,1\}$. System (2) involves a non-negative density $\rho(t,x) > 0$ and a velocity $U(t,x)$ which are assumed to be bounded. Obviously, since system (2) is only based on two equations and three unknowns, ρ or U have to be specified. In the sequel, we focus on the specific class of solutions described in appendix 6.2. The latter possesses non-uniform but smooth profiles for the density and for the velocity. We recall that we also restrict our study here to scalar $\phi(t,x)$ that are on the form of Heaviside functions, and that are therefore equal to zero or one at every point (t,x).

2.1   The Glimm scheme

Let us consider the domain $x \in [0,1]$ meshed with N_c uniform cells of length $\Delta x = 1/N_c$, and let us choose a time-step Δt. In each cell $i \in 1, N_c$, the approximated value of the scalar ϕ at time $t^n = n\Delta t$ is denoted by ϕ_i^n. Starting from the sequence $\{\phi_i^n, i \in 1, N_c\}$ that approximates the solution at time t^n, the updated sequence $\{\phi_i^{n+1}, i \in 1, N_c\}$ approximating the solution at time $t^{n+1} = t^n + \Delta t$ is obtained by setting:

$$\phi_i^{n+1} = \begin{cases} \phi_{i-1}^n, & \text{if} \quad \omega^n \in [0, h_{i-1/2}^n], \\ \phi_i^n, & \text{if} \quad \omega^n \in [h_{i-1/2}^n, h_{i+1/2}^n], \\ \phi_{i+1}^n, & \text{if} \quad \omega^n \in [h_{i+1/2}^n, 1], \end{cases} \tag{3}$$

where $h_{i-1/2}^n = U_{i-1/2}^n \Delta t/\Delta x$ and $h_{i+1/2}^n = 1 + U_{i+1/2}^n \Delta t/\Delta x$, with $U_{i-1/2}^n = U(t^n, (i-1)\Delta x)$ the velocity at the interface between the cells $i-1$ and i at time t^n. The quantity ω^n is a quasi-random number chosen in $[0,1]$ following an uniform law. In scheme (3), we follow the proposition given in[3, 5] by choosing at each iteration the same value ω^n for all the cells. Moreover, as proposed in [5], the quasi-random number ω^n is chosen in low discrepancy sequences built using the Halton-Van der Corput algorithm.

The quantities $U_{i+1/2}^n \Delta t/\Delta x$ can be positive or negative. Obviously, if $h_{i+1/2}^n > 1$ (resp. $h_{i-1/2}^n < 0$), which means that $U_{i+1/2}^n > 0$ (resp. $U_{i-1/2}^n < 0$), the last (resp. first) condition in (3) can not be fulfilled. In these cases, ϕ_i^{n+1} can not be updated using ϕ_{i+1}^n (resp. ϕ_{i-1}^n). It should be mentioned that in order to have the possibility to update ϕ_i^{n+1} using ϕ_i^n, i.e. with the second case of (3), the time step Δt has to be chosen so that $h_{i-1/2}^n < h_{i+1/2}^n$. This condition is a constraint only when $U_{i-1/2}^n > 0$ and $U_{i+1/2}^n < 0$. It can thus be written:

$$(|U_{i-1/2}^n| + |U_{i+1/2}^n|)\Delta t < \Delta x.$$

The time-step should also fulfill $|h_{i-1/2}^n| < 1$ for all i, which leads to:

$$|U_{i-1/2}^n|\Delta t < \Delta x.$$

These constraints can be fulfilled by using the following sufficient CFL condition for the time-step Δt:

$$\Delta t < \frac{\Delta x}{2 \ max_i \left((|U_{i-1/2}^n|) \right)}, \tag{4}$$

which obviously only makes sense if there exists at least one velocity $U_{i-1/2}^n \neq 0$.

The properties of the Glimm scheme (3) have been studied for instance in [13, 14, 18]. We propose here to summarize theses properties.

- The scheme is conservative in a statistical sense.

- The scheme is entropy dissipative in a statistical sense.

- The approximated solution for the scalar remains equal to zero or one.

- The scheme is first order in a statistical sense.

In the following section 2.4, some convergence results are presented with respect to the analytical solution given in appendix 6.2.

We present here a simple result that illustrates the statistical behavior of the Glimm scheme. If we assume that U is uniform a positive, $U(t,x) = U_0 > 0$, the scheme (3) simplifies in:

$$\phi_i^{n+1} = \phi_{i-1}^n \mathbb{K}_{\omega^n \in [0,h_0]} + \phi_i^n \mathbb{K}_{\omega^n \in [h_0,1]}, \tag{5}$$

where $h_0 = U_0 \Delta t / \Delta x$. Let us apply the statistical expectation $E(.)$ to formula (5), it yields:

$$E(\phi_i^{n+1}) = E(\phi_{i-1}^n \mathbb{K}_{\omega^n \in [0,h_0]}) + E(\phi_i^n \mathbb{K}_{\omega^n \in [h_0,1]}).$$

Assuming that the random choice for ω^n is independent from the values of $\{\phi_i^n, i \in 1, N_c\}$, the two terms on the right hand side can be written as two products of the expectations:

$$E(\phi_i^{n+1}) = E(\phi_{i-1}^n) E(\mathbb{K}_{\omega^n \in [0,h_0]}) + E(\phi_i^n) E(\mathbb{K}_{\omega^n \in [h_0,1]}).$$

Now, if the probability law for ω^n is uniform on $[0,1]$, we get:

$$E(\phi_i^{n+1}) = E(\phi_{i-1}^n) h_0 + E(\phi_i^n)(1 - h_0).$$

This formula corresponds to the update formula obtained with the classical Upwind scheme for the expectation sequence $\{E(\phi_i^n), i \in 1, N_c\}$. Concerning the probabilistic law for ω^n, the independence between ω^n and the values $\{\phi_i^n, i \in 1, N_c\}$ together with the equidistributed and low-discrepancy properties are essential in order to obtain a convergent scheme. This point is illustrated in section 2.4.

Remark. At last, it should be mentioned that for our specific problem, the Glimm scheme (3) can be written as a fractional step scheme when $h_{i-1/2}^n < h_{i+1/2}^n$:

$$\phi_i^{n+1,-} = \begin{cases} \phi_{i-1}^n, & \text{if } \omega^n \in [0, h_{i-1/2}^n], \\ \phi_i^n, & \text{otherwise,} \end{cases} \quad \text{and then} \quad \phi_i^{n+1} = \begin{cases} \phi_{i+1}^n, & \text{if } \omega^n \in [h_{i+1/2}^n, 1], \\ \phi_i^{n+1,-}, & \text{otherwise.} \end{cases} \tag{6}$$

The first step of (6) is then associated to interface $i - 1/2$ and the second step to interface $i + 1/2$. Note that ω^n has to be the same for both steps.

2.2 The Glimm Random Update (GRU)

As depicted for instance in [17, 16], the Glimm scheme can be extended to multi-dimensional meshes, provided that these meshes are structured. The schemes proposed in [17, 16] are also based on Glimm's ideas and they have been assessed on complex two-dimensional two-phase flow problems. In particular, Glimm's ideas have been applied to maintain sharp interfaces between the phases and to avoid "non-physical" mixtures produced by the numerical diffusion of the front. With these methods the mass fraction describing the mixture remains an indicator function as expected. However, a fractional step approach that alternates the spatial directions is used, which restricts the method to structured meshes. On unstructured meshes, it seems difficult to propose a consistent scheme based on the Glimm scheme of section 2.1 [5]. Keeping in mind that we are interested by multi-dimensional configurations, we propose here an other scheme based on the idea of random choices. The main idea is that on unstructured meshes, despite its numerical diffusion, the Upwind scheme always succeeds in following the exact discontinuity. Indeed, the Upwind scheme is associated with an important numerical diffusion and, in the neighborhood of the front, it produces approximated values that are intermediate between 0 and 1 [1]. Nevertheless, the exact front is always located in the domain where approximated values obtained with the Upwind scheme belong to $]0,1[$. On the basis of this remark, we thus propose to adapt the Upwind scheme following Glimm's ideas and [7].

2.2.1 Algorithm for the GRU step

We assume that at time t^n, for all cells i we have $\phi_i^n \in \{0,1\}$. The value of the scalar ϕ_i^n is first updated into $\phi_i^{n+1,*}$ thanks to the following Upwind scheme based on the analytical solution for ρ and U:

$$\begin{cases} \rho_i^{n+1,*} \phi_i^{n+1,*} = \rho_i^n \phi_i^n - \frac{\Delta t}{\Delta x} \left(Q_{i+1/2}^n \phi_{i+1/2}^n - Q_{i-1/2}^n \phi_{i-1/2}^n \right), \\ \rho_i^{n+1,*} = \rho_i^n - \frac{\Delta t}{\Delta x} \left(Q_{i+1/2}^n - Q_{i-1/2}^n \right), \end{cases} \tag{7}$$

---

[1]Obviously, the linear advection problem solved on uniform meshes with the optimal CFL condition is a very specific problem. We consider here more general situations.

with the mass fluxes: $Q^n_{i+1/2} = \rho^n_{i+1/2} U^n_{i+1/2}$. In our particular case, the density and the velocity are given by the explicit formula of section 6.2 and we thus choose: $\rho^n_{i+1/2} = \rho(t^n, (i-1)\Delta x)$, $U^n_{i-1/2} = U(t^n, (i-1)\Delta x)$ and $\rho^n_i = \rho(t^n, (i-1/2)\Delta x)$. Moreover, it should be noted that in general $\rho^{n+1,*}_i$ may be different from $\rho^{n+1}_i = \rho(t^n + \Delta t, (i-1/2)\Delta x)^2$. The interfacial value $\phi^n_{i+1/2}$ is then:

$$\phi^n_{i+1/2} = \begin{cases} \phi^n_i, & \text{if } U^n_{i+1/2} > 0 \\ \phi^n_{i+1}, & \text{otherwise.} \end{cases} \tag{8}$$

This scheme is based on the classical Upwind scheme but it embeds the analytical solutions for ρ and U. It is named Upwind in the following but it should not be mistaken with the classical Upwind scheme. Some properties of this scheme are given in appendix 6.1, in particular it is proven that it is monotonicity preserving for ϕ. Therefore, considering a positive time-step $\Delta t > 0$ that fulfills (4), the cells that were at time t^n on each side of a discontinuity contain at the end of this first time-step an approximated value of ϕ which lies in $]0, 1[$.

The second step of the present scheme consists therefore in projecting these values on $\{0, 1\}$. For that purpose, we consider a quasi-random number ω^n that follows a uniform law in $[0, 1]$. The projection step then simply consists in updating $\phi^{n+1,*}_i$ according to:

$$\phi^{n+1}_i = \begin{cases} 1, & \text{if } \omega^n \in [0, \phi^{n+1,*}_i], \\ 0, & \text{otherwise.} \end{cases} \tag{9}$$

This last step of the algorithm seems quite naive (and despicable), but it results in a numerical scheme that in terms of accuracy and convergence rate performs as well as the Glimm scheme of section 2.1 for one-dimensional settings. Moreover, it will be seen in section 4 that this schemes behaves very well on unstructured meshes. Indeed, it takes advantage of the underlying Upwind scheme which handles correctly unstructured meshes. It is an important point to be quoted that the projection (9) does not restrict to the Upwind scheme for the first step. It remains very general, as shown in the section 3 or appendix 6.4. In the following, the projection (9) of the present algorithm is nicknamed GRU (for Glimm Random Update). The scheme above, based on the Upwind scheme and the GRU step, will be nicknamed Upwind-GRU.

At last, it should be noticed that when applying the statistical expectation $E(.)$ to formula (9), it comes that:

$$E(\phi^{n+1}_i) = E(\mathbb{1}_{\omega^n \in [0, \phi^{n+1,*}_i]}) = \phi^{n+1,*}_i.$$

In that sense, the Upwind-GRU scheme statistically converges towards the Upwind scheme, as the Glimm scheme.

2.2.2 A monotonicity property

The GRU step leads to a very interesting property when associated with a first step based on a monotonicity preserving scheme. Let us assume that this is the case: the Upwind scheme of the first step above is replaced by any monotonicity preserving scheme with a "two-point" flux. For the sake of simplicity (and without any loss of generality), let us also assume that at time-step t^n the discrete values of the scalar ϕ, $(\phi^n_k)_{k \in 1, N_c}$, are equal to 1 if $k \leq i$ and 0 otherwise. Figure 1a presents a sketch of such a situation. If the first step if computed using a monotonicity preserving scheme based on a "two-point" numerical flux, then we get at the end of this first step that :

$$\phi^{n+1,*}_{i-1} \geq \phi^{n+1,*}_i \geq \phi^{n+1,*}_{i+1} \geq \phi^{n+1,*}_{i+2},$$

and

$$\forall k < i-1, \ \phi^{n+1,*}_k = 1, \quad \text{and} \ \forall k > i+1, \ \phi^{n+1,*}_k = 0.$$

Then, choosing the same pseudo-random number ω_n to update all the cells in the GRU step implies that the monotony of the sequence of the discrete values of the scalar ϕ is conserved. In other words, we have:

$$\phi^{n+1}_{i-1} \geq \phi^{n+1}_i \geq \phi^{n+1}_{i+1} \geq \phi^{n+1}_{i+2},$$

and

$$\forall k < i-1, \ \phi^{n+1}_k = 1, \quad \text{and} \ \forall k > i+1, \ \phi^{n+1}_k = 0.$$

This is an important property. Indeed, the consequence is that no inclusion can be added by the GRU step when the first step is performed through a monotonicity preserving scheme. This example also highlights that the GRU step consists in fact in choosing the new front location among the possible interfaces $i-1/2$, $i+1/2$ and $i+3/2$, see figure 1a.

---

[2]Indeed, thanks to a Taylor expansion, one can easily obtain that: $\rho^{n+1,*}_i - \rho^{n+1}_i = o(\Delta t)$. See appendix 6.1 for details.

2.2.3 Pathological cases: front disapperance

We focus now on a pathological situation for the GRU step when associated with a monotonicity preserving scheme, as depicted above. Such a case is described in figure 1b. If at time-step t^n, $\phi_k^n = 1$ only for $k \in \{i, i+1\}$, then at the end of the first step we will get that: $\forall k \in 1, N_c$, $\phi_k^{n+1,*} < 1$. Hence, if ω^n is chosen such that:

$$\omega^n > \max_{k \in 1, N_c} (\phi_k^{n+1,*}),$$

at the end of the GRU step we get:

$$\forall k \in 1, N_c, \ \phi_k^{n+1} = 0.$$

This remark shows that the propagation of a thin front may lead to its disappearance. In the case depicted here, the front disappears with probability $1 - \max_{k \in 1, N_c} (\phi_k^{n+1,*})$. Obviously, if such a situation is encountered, one should refine the mesh to avoid front disappearance.
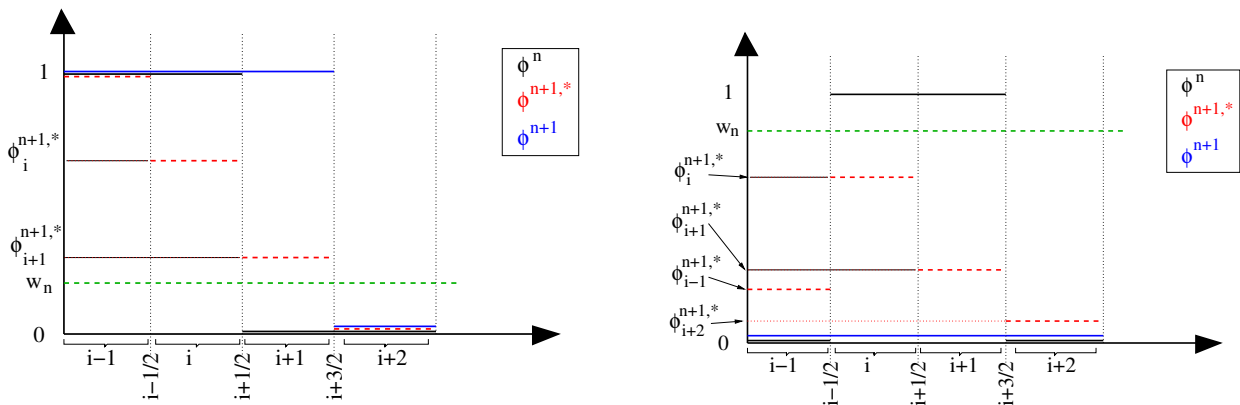
(a) Classical front propagation with the GRU step considering a first step based on a monotonicity preserving scheme. The initial front is located at interface $i + 1/2$. For a first step of the algorithm based on a monotonicity preserving scheme, the GRU step consists in choosing on which interface $i-1/2$, $i+1/2$ or $i+3/2$ the new front could be located at time t^{n+1}.

(b) Pathological case: example of the GRU step considering a first step based on a monotonicity preserving scheme. The scalar a time t^n is equal to 1 on the two cells i and $i + 1$. After the GRU step, this two cells may be updated to 0 depending ω^n. In such case, the scalar front "disappears" from the domain.

Figure 1: Example of the behavior of the GRU step when the first step is based on a monotonicity preserving scheme.

2.3 A link between the Glimm's scheme and the Upwind-GRU scheme

In this section we exhibit a link between the Glimm's scheme and the Upwind-GRU scheme described in the previous sections. This link only holds for a particular class of solutions. In system (2), a constant and uniform density $\rho(t, x) = \rho_0 > 0$ is imposed and the velocity field $U(t, x)$ is assumed to be constant, non-negative and continuous. We then consider an initial condition for the scalar quantity such that $\phi(t, x) = 1$ if $x < x_0$ and $\phi(t, x) = 0$ otherwise. Let us assume that on a given uniform mesh, the approximated solution at time t^n is such that there exists an index i_0 such that:

$$\phi_j^n = \begin{cases} 1, & \text{if } j < i_0, \\ 0, & \text{otherwise.} \end{cases}$$

Since the velocity is non-negative, the Glimm's scheme of section 2.1 then gives that:

$$\forall j \neq i_0, \ \phi_j^{n+1} = \phi_j^n, \quad \text{and} \quad \phi_{i_0}^{n+1} = \begin{cases} 1, & \text{if} \quad \omega^n \in [0, h_{i_0-1/2}^n], \\ 0, & \text{if} \quad \omega^n \in [h_{i_0-1/2}^n, 1], \end{cases} \tag{10}$$

where $h_{i_0-1/2}^n = U_{i_0-1/2}^n \Delta t / \Delta x$. Considering the same problem, the Upwind-GRU scheme of section 2.2 leads to the update:

$$\forall j \neq i_0, \ \phi_j^{n+1} = \phi_j^n, \quad \text{and} \quad \phi_{i_0}^{n+1} = \begin{cases} 1, & \text{if} \quad \omega^n \in [0, \phi_{i_0}^{n+1,*}], \\ 0, & \text{if} \quad \omega^n \in [\phi_{i_0}^{n+1,*}, 1], \end{cases} \tag{11}$$

where $\phi_{i_0}^{n+1,*} = U_{i_0}^n \Delta t/\Delta x$. As a consequence, when the velocity profile is locally uniform around the front location, we get $\phi_{i_0}^{n+1,*} = h_{i_0-1/2}^n$, which means that the Glimm's scheme and the Upwind-GRU scheme coincide for this very peculiar problem. Moreover, when the velocity is not locally uniform we have $\phi_{i_0}^{n+1,*} \neq h_{i_0-1/2}^n$, but thanks to the continuity of the velocity profile with respect to x, we have:

$$|U_{i_0}^n - U_{i_0-1/2}^n| \xrightarrow[\Delta x \to 0]{} 0,$$

and thus

$$|\phi_{i_0}^{n+1,*} - h_{i_0-1/2}^n| \xrightarrow[\Delta x \to 0]{} 0.$$

In other words, when the mesh is refined, the Glimm's scheme and the Upwind-GRU scheme tends to give the same update-formula. Such a behavior can be observed in the next section, in particular when considering figure 2. The gap between the convergence curves obtained for the two schemes decreases to zero when the mesh size tends towards zero.

2.4 Numerical results

In the following we consider the analytical solution proposed in section 6.2 with the parameters $x_0 = 0.3$, $U_0 = 2$, $R_0 = 2$, $B_0 = -1$, and with the final time $t = 0.2$ (see figure 29 for a plot of the solution over $[0, 1]$). The domain $[0, 1]$ is discretized using uniform cells and the time-step is chosen in accordance with a CFL-number equal to $1/2$. Thanks to our choice for the parameters of the analytical solution, the velocity U is constant and it is decreasing along x. The time-step is then set to: $\Delta t = CFL \, \Delta x/U(t, x = 0)$, where Δx denotes the mesh size.

In a practical point of view, the random number ω^n needed for iteration n in the Glimm scheme and in the Upwind-GRU scheme is chosen as the nth element of a Halton-Van der Corput low-discrepancy sequence with the parameters (K_1, K_2) (see appendix 6.5 for a detailed algorithm). Each couple of parameters leads to a different quasi-random sequence. For each test case and for each mesh size, the approximated solutions have been computed here using several (different) Halton-Van der Corput (determined by the couple of parameters (K_1, K_2)). Thus, the different couples (K_1, K_2) produce approximated solutions that may be different for a given mesh size and for a given test case. This set of Halton-Van der Corput sequences is chosen as follow. If we denote by $\mathcal{P}(n)$ the sequence containing the n first prime numbers greater or equal to 3, the couples that are used in the sequel are all the couples $(K_1, K_2) \in \mathcal{P}(n) \times \mathcal{P}(n)$ such that $K_2 < K_1$. In particular, the results of the present section have been computed for $\mathcal{P}(8) = \{3, 5, 7, 11, 13, 17, 19, 23\}$, and therefore 28 different couples (K_1, K_2) have been used for each mesh size and for each test case.

For each mesh size and for each couple (K_1, K_2), the L_1−error between the approximated solution obtained with the Glimm or Upwind-GRU scheme and the analytical solution is computed. Then, for each mesh size, the L_1−error obtained for all the couple (K_1, K_2) is averaged. We then get an average error estimate for each mesh size. In figure 2 the red and blue curves respectively show the statistical convergence curve for the Glimm scheme and the Upwind-GRU scheme of the previous sections. As a comparison, the convergence curve for the Upwind scheme is also plotted. It can be observed that the Glimm scheme and the Upwind-GRU scheme have a greater accuracy together with a convergence rate of 0.85 for the meshes considered. The Upwind scheme reaches rapidly its asymptotic convergence rate of 0.5, whereas the Glimm scheme and the Upwind-GRU scheme have not yet reached a convergence rate of 1.

An important point in the Glimm scheme is that the sequence used to update the value in a cell has to be an equidistributed low-discrepancy sequence [5]. In order to illustrate that point, we present in figure 2 the results obtained with the Glimm scheme and with periodic sequences obtained from a Halton-Van der Corput sequence with 500 items. With such periodic sequences, it can be shown that the Glimm scheme does not converge. This can be easily explained. Once the scheme has performed 500 time-iterations, the following values of ω^n are no more independent of the previous values of ϕ_i^j for $j < n$ and the sequence is not equidistributed. In the present case, with the choice of parameters for the analytical solution, the contact discontinuity travels from $x_0 = 0.3$ to $x = 0.583$. Thanks to our CFL condition of $1/2$ (see also section 2.1), it means that the first loop over the 500 items of the periodic sequence is achieved for a mesh that contains $500/2/(0.583 - 0.3) \sim 880$ cells. in figure 2, this value of 880 cells corresponds to an abscissa of $\log(1.0/880) \sim -6.8$. It can clearly be observed that below that mere abscissa, the converge curve flattens. Obviously, the same behavior can be observed for the Upwind-GRU scheme.
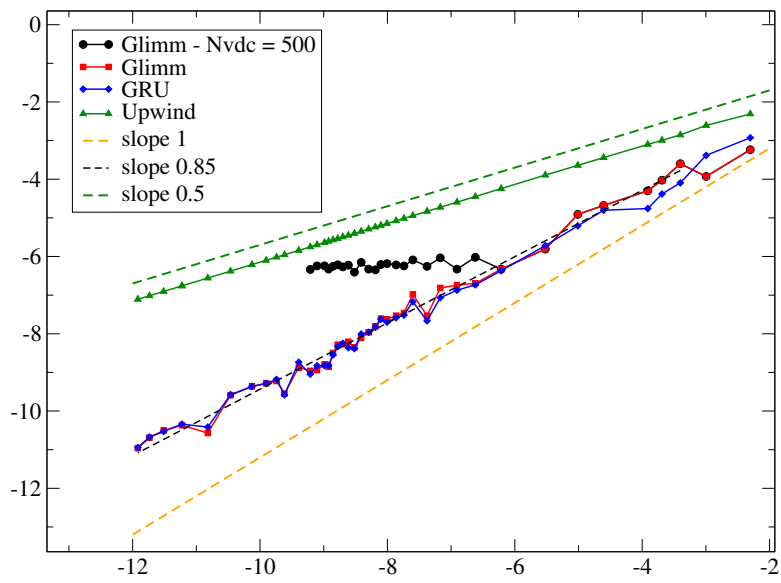
Figure 2: Convergence curves for: the Upwind scheme (green), the Glimm scheme (red), the Glimm scheme with a truncated quasi-random sequence (black), and the Upwind-GRU scheme (blue). The meshes contain from 10 to 150000 cells (except for the black curve).

3 Application to the Euler system of equations with scalar advection

In the two previous sections, the GRU step has been tested on simple problems where the velocity field and the density were exactly known (through analytical solutions). These situations correspond to the optimal setting to get a high convergence rate for the numerical approximations of the scalar quantity. In more complex settings, the scalar quantities are updated with the help of the density and the velocity that are also approximated by a numerical scheme. Hence, for these situations, the convergence rate and the accuracy of the numerical approximations for the scalar quantity are limited by those of the other variables. In the present section, we focus on the Euler system of equations and we consider explicit first-order schemes.

We introduce a simple two-phase model based on the Euler set of equations:

$$\begin{cases} \partial_t \left(\rho \phi \right) + \partial_x \left(\rho U \phi \right) = 0, \\ \partial_t \left(\rho y \right) + \partial_x \left(\rho U y \right) = 0, \\ \partial_t \left(\rho \right) + \partial_x \left(\rho U \right) = 0, \\ \partial_t \left(\rho U \right) + \partial_x \left(\rho U^2 + P \right) = 0, \\ \partial_t \left(\rho E \right) + \partial_x \left(U(\rho E + P) \right) = 0, \end{cases} \tag{12}$$

where y denotes the mass fraction, $E = e + U^2/2$ is the total energy with e the internal energy. The pressure law $(y, \rho, e) \mapsto P(y, \rho, e)$ is obtained as a mixture of perfect gases [11, 16], it reads:

$$P(y, \rho, e) = (y\gamma_1 + (1 - y)\gamma_2 - 1)\rho e. \tag{13}$$

The parameters γ_1 and γ_2 are the adiabatic coefficients of each gas. This mixture pressure law is in agreement with the mixture entropy $s(y, \rho, e) = e\rho^{(y\gamma_1 + (1-y)\gamma_2) - 1}$. As in the test case of section 2 the quantities ϕ and y are advected by the contact wave U.

In order to compute numerical approximations of system (3.2), we use the two-step approach proposed in the previous sections: the first step of the algorithm is based on the VFRoe-ncv scheme using the variable (ϕ, y, U, P, s) [12]; then the GRU step (9) is performed. We recall here that the mixture pressure law (13) for $\gamma_1 \neq \gamma_2$ does not allow to preserve the uniform profiles of the velocity and pressure across the contact wave, see [10]. On the basis of the model (3.2) with (13), we investigate here four test cases. These test cases are based on Riemann problems involving a $U - c$ rarefaction wave and a $U + c$ shock wave, where c denotes the sound speed. Figure 3 represents the wave structure of the test cases retained here. Moreover, we are only interested here in a convergence study for the scalar quantities. We thus only need to compute the exact solution for the speed of the contact wave, which amounts to find intermediate states l and r for the velocity. We recall that we have here $U_l = U_r$. For each test case, the values of all the intermediate states and the value of the speed of the contact wave are gathered in tables 1, 2 and 3. Computation of the analytical solutions of Riemann problems for the Euler system of equations can be found for instance in [20].
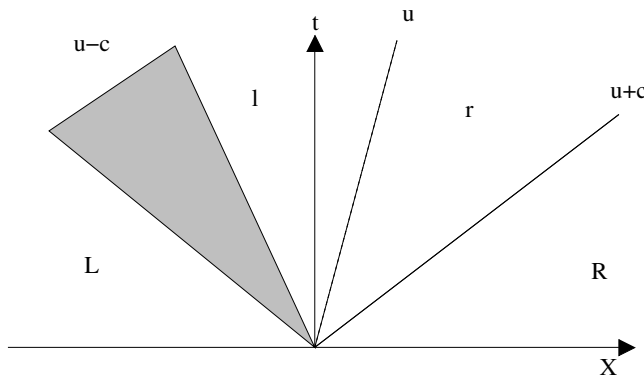

Figure 3: Sketch of the four Riemann problems. The four intermediate states L, l, r and R are respectively separated by a rarefaction wave $U - c$, a contact wave U and a shock wave $U + c$.

3.1 Single-phase flow test case

In these test cases, the GRU step only concerns the scalar ϕ. For the two first test cases we assume $\gamma_1 = \gamma_2 = 1.4$. Figure 4 shows the approximated solutions of these two Riemann problems and tables 1 and 2 gather the values

of the intermediate states. The first Riemann problem (on the left column, in red, in figure 4) is associated with a low-speed contact wave; whereas the second one corresponds to a high-speed contact wave (on the right column, in blue, in figure 4). It should be observed that the pressure and velocity profiles are uniform through the contact wave. This is a well known behavior due to the specific VFRoe-ncv scheme used here, see [10] for details.

	L	l	r	R
ϕ	1.0	1.0	0.0	0.0
y	1.0	1.0	0.0	0.0
ρ	0.9	0.928391167192429	0.94	0.969655918557038
U	0	11.65829027971115	11.65829027971115	0
P	$9.0 \ 10^4$	$9.4 \ 10^4$	$9.4 \ 10^4$	$9.81778624359525 \ 10^4$
contact	11.65829027971115			

Table 1: Intermediate states for the different variables for the single-phase flow problem ($\gamma_1 = \gamma_2 = 1.4$) with a low-speed contact wave.

	L	l	r	R
ϕ	1.0	1.0	0.0	0.0
y	1.0	1.0	0.0	0.0
ρ	0.125	0.235294117647059	0.5	1.14041408418208
U	0	237.1708245126285	237.1708245126285	0
P	$1.0 \ 10^4$	$2.5 \ 10^4$	$2.5 \ 10^4$	$7.92993456572169 \ 10^4$
contact	237.1708245126285			

Table 2: Intermediate states for the different variables for the single-phase flow problem ($\gamma_1 = \gamma_2 = 1.4$) with a high-speed contact wave.
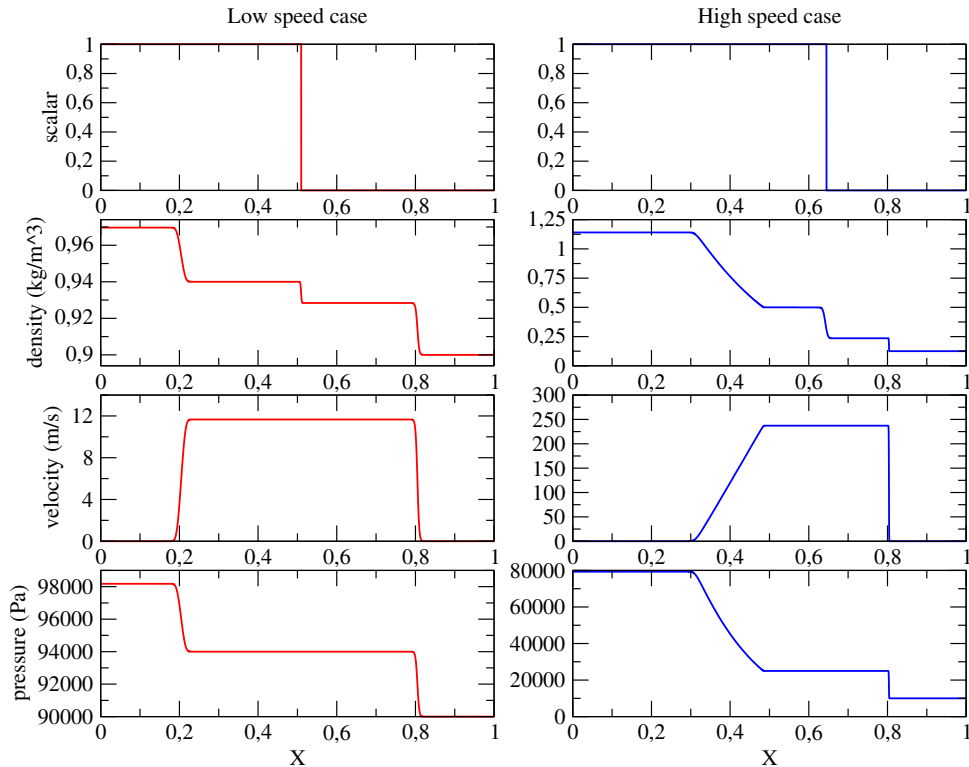

Figure 4: Approximated solutions obtained with the VFRoe-ncv-GRU scheme for 5000 cells. The columns on the left show the low-speed test case and the columns on the right show the high-speed test case. The initial discontinuity was located at $x = 0.5$.

We recall now some classical results for the convergence rate of the VFRoe-ncv scheme with variable (ϕ, y, U, P, s) when applied to system (3.2) with $\gamma_1 = \gamma_2$, see [11]. The convergence rate for the velocity U

and the pressure P is equal to 1, and the convergence rate for the density ρ and the scalar quantities ϕ and y is equal to $1/2$. In practice, the measured convergence rates for U and P is close to $0.8 - 0.85$. In the present test case, the variables ϕ and y are discretized using a conservative form that involves the density. Since the approximated solutions of ϕ and y then depends on the approximated solutions of the density, we cannot expect these variables to converge faster than $1/2$ in the general case. In order to get a better convergence rate for the scalar ϕ when using the GRU step, one could consider its equation in a non-conservative form and choose to use, for instance, the Lax-Friedrichs scheme recalled in section 6.4. Then the update of ϕ would not rely on the density but on the sole velocity. Since the latter converge at the effective order of $0.8 - 0.85$, we could expect the same convergence rate for ϕ, as in section 6.4. Nevertheless, it should be mentioned that using a non-conservative form for ϕ must be handled with care. When the velocity field is smooth at the points where the scalar ϕ is discontinuous, no additional difficulty arises; but if both U and ϕ are discontinuous at a same point, one as to deal with the non-conservative product $U\partial_x(\phi)$.

The convergence curves are plotted in figure 5. For the low-speed test case, the convergence rate is still over the expected rate of $1/2$ for the considered meshes, whereas for the high-speed test case the order $1/2$ is reached on coarse meshes. It can be observed that the GRU step is more efficient for the low-speed test case. Indeed, for the VFRoe-ncv scheme the time-step is chosen in accordance with the CFL condition based on the $U \pm c$ waves. As a consequence, the more the contact wave travels slowly with respect to the $U \pm c$ waves, the less accurate the VFRoe-ncv scheme is for approximating the contact wave. In this low-speed case, the displacement of the approximated front is slow and numerical diffusion prevails. When considering the GRU step, the initial profile for the scalar quantity ϕ is not diffused. Hence, the error between the approximated solutions and the exact solution is only due to the localization of the approximated front. On the contrary, for the high-speed case, the numerical diffusion is less prevailing that the front displacement. Therefore, the GRU step less improves the approximated solutions of the VFRoe-ncv scheme for the scalar quantity ϕ.

Considering the same test case, the first order finite volumes scheme is now replaced by a classical second order scheme. The VFRoe-ncv fluxes are now combined with a MUSCL scheme for slope reconstruction and a minmod slope limiter (see [21] among others). This is a basic second order scheme which is conservative and that is monotonicity preserving for the scalar quantity ϕ. It is well-known that an effective convergence rate of $2/3$ is expected for ϕ, see [11] for instance. The convergence curves are plotted in figure 6. With the MUSCL scheme the convergence rate of $2/3$ is recovered, whereas the GRU step still allows to improve the accuracy. Moreover, a convergence rate of 0.85 is obtained, as with the first order scheme (see figure (5)). For this one-dimensional test case, the GRU step still improves the approximated solution, even if it is less significant than for the first order scheme.
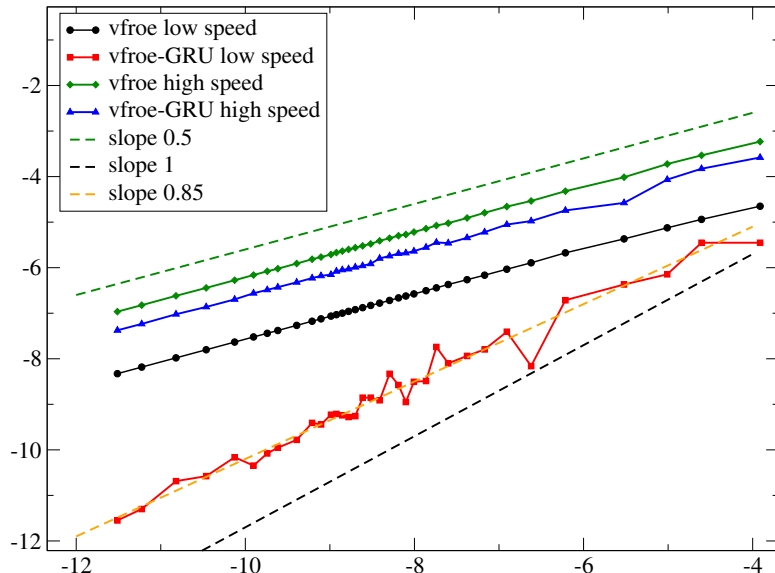

Figure 5: Convergence curves for the scalar ϕ for the single-phase Euler test problems. The black and green curves correspond to the VFRoe-ncv scheme without GRU step. The red and blue curves correspond to the VFRoe-ncv scheme with a GRU update for the scalar ϕ. The meshes contain from 10 to 100000 cells.
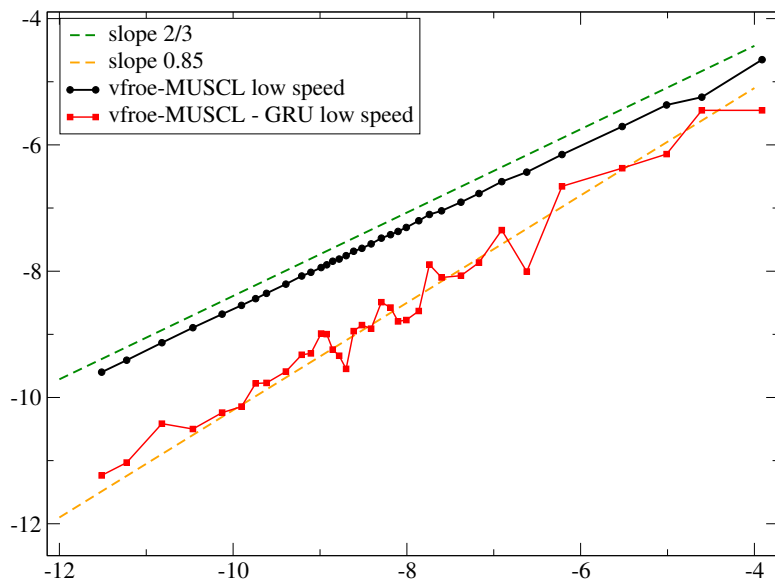
Figure 6: Convergence curves for the scalar ϕ for the single-phase Euler test with a low-speed contact wave. The black curve corresponds to the MUSCL scheme without GRU step. The red curve corresponds to the MUSCL scheme with a GRU update for the scalar ϕ. The meshes contain from 10 to 100000 cells.

3.2 Two-phase flow test case

We consider here the Riemann problem with the intermediate states of table 3 obtained for $\gamma_1 = 1.4$ and $\gamma_2 = 5$. Since the mass fraction is equal to zero on the right of the contact wave and to one on the left, this test case can be seen as the interaction of a shock wave on the interface between to immiscible fluids. It should be emphasized that the analytical profile for U and P should be uniform across the contact wave because they are Riemann invariant of the U-contact wave. Unfortunately, due to the mixture EOS (13), the VFRoe-ncv scheme does not preserve these invariants on approximated solutions for coarse meshes, see for instance [11, 10]. In figure 7, the left column shows the approximated solutions for three meshes. The velocity and the pressure profiles are clearly not uniform across the contact waves for these coarse meshes. Nevertheless, it should be noted that the approximated solutions converge towards the exact solution and, thus, towards uniform profiles for U and P.

Two numerical tests, denoted by A and B, are reported here on the basis of the Riemann problem described above. For both tests, the first step is computed using the VFRoe-ncv scheme with variable (ϕ, y, U, P, s). Then, for test case A, the GRU step is applied on the sole scalar quantity ϕ, whereas for test case B the GRU step is applied to ϕ and y. Note that for test case B, we have in fact $\phi = y$. The approximated solutions for test cases A and B are plotted in figure 7.

For test case B, it could seem appealing to apply the GRU step to the mass fraction y in order to improve the accuracy on the contact wave. But this clearly leads to a non-stable scheme, as also shown by the convergence curve of figure 8. Indeed, the GRU step on y implies a conservative update of the pressure which generates pressure oscillations. Let us assume that the first step leads to a value $y_i^{n+1,*}$ of y in cell i such that $0 < y_i^{n+1,*} < 1$. Then, the GRU step applied to y gives the update formula:

$$\begin{cases} y_i^{n+1} & \neq y_i^{n+1,*} \\ \rho_i^{n+1} & = \rho_i^{n+1,*} \\ (\rho e)_i^{n+1} & = (\rho e)_i^{n+1,*} \end{cases} \tag{14}$$

When focusing on the update of the pressure, equations (14) can be written:

$$e(y_i^{n+1}, \rho_i^{n+1}, P_i^{n+1}) = e(y_i^{n+1,*}, \rho_i^{n+1}, P_i^{n+1,*}),$$

which thanks to (13) gives the pressure update:

$$P_i^{n+1} = P_i^{n+1,*} \frac{(y_i^{n+1}\gamma_1 + (1 - y_i^{n+1})\gamma_2 - 1)}{(y_i^{n+1,*}\gamma_1 + (1 - y_i^{n+1,*})\gamma_2 - 1)}. \tag{15}$$

Therefore, when $y_i^{n+1} \neq y_i^{n+1,*}$, the pressure update (15) leads to strong variations of the pressure around the contact wave. This behavior is clearly illustrated in figure 7 and in figure 8, where the pressure oscillations lead to a non-convergence.

For test case A, figure 8 shows that the scheme converges toward the analytical solution. But, it can also be noted that the accuracy improvement of the GRU step is lower than for the single-phase low-speed test case depicted above in figure 5. This is due to the fact that for the present two-phase flow, the velocity profile presents a strong discontinuity on coarse meshes. This discontinuity separates two different values of velocity. Depending on the random numbers, the GRU step then moves the approximated front on both side of this discontinuity. The convection step is thus achieved for ϕ with a velocity that highly fluctuates. The global accuracy is thus lower, and the convergence rate is closer from the expected rate of convergence of $1/2$.

	L	l	r	R
ϕ	1.0	1.0	0.0	0.0
y	1.0	1.0	0.0	0.0
ρ	0.9	0.907860262008734	0.94	0.955687784544004
U	0	6.20322806932314	6.20322806932314	0
P	$9.0\ 10^4$	$9.4\ 10^4$	$9.4\ 10^4$	$9.62035963634646\ 10^4$
contact	6.20322806932314			

Table 3: Intermediate states for the different variables for the two-phase flow problem ($\gamma_1 = 1.4$ and $\gamma_2 = 5$).
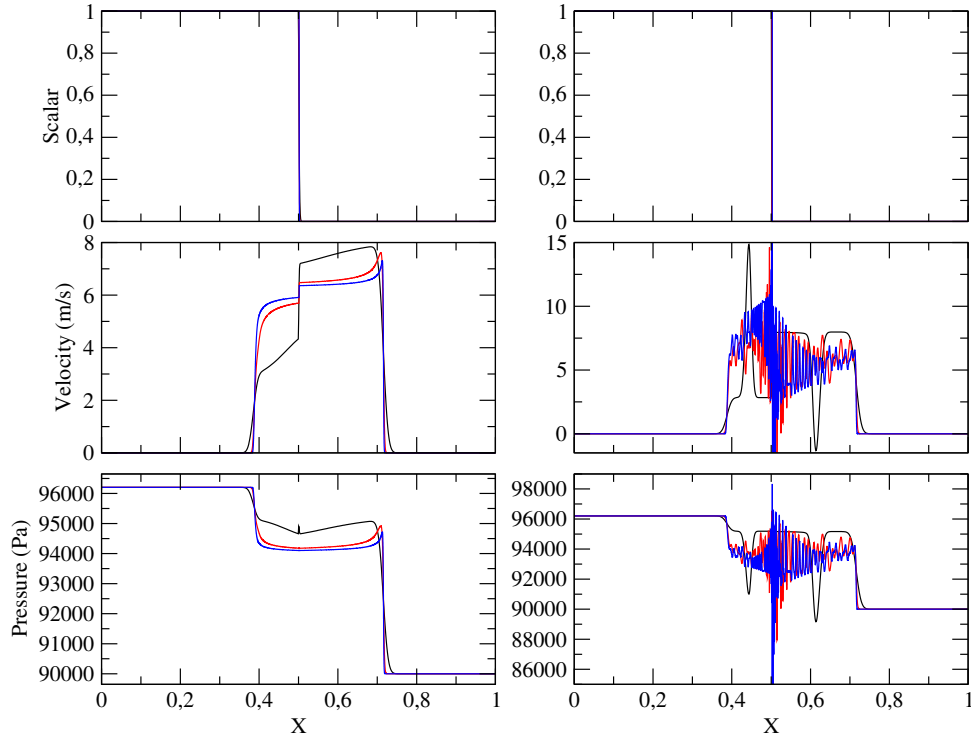
Figure 7: Approximated solutions obtained with the VFRoe-ncv scheme for 1000 (black lines), 10000 (red lines) and 30000 (blue lines) cells. The columns on the left show the approximated solutions for the two-phase Euler model without GRU step for the mass fraction (case A), and the columns on the right show the approximated solutions for the two-phase Euler model with GRU step for the mass fraction (case B). The initial discontinuity was located at $x = 0.5$.
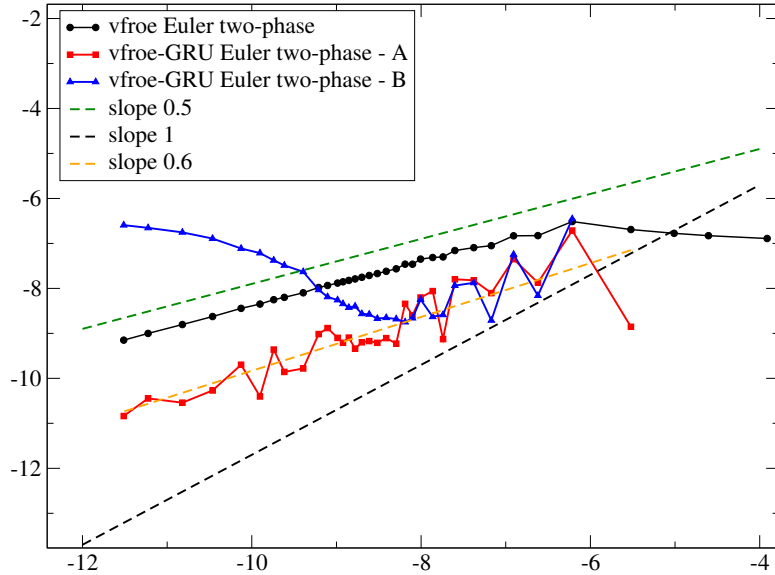

Figure 8: Convergence curves for the scalar ϕ (test case A) or y (test case B) for the two-phase Euler test problem. The black curve corresponds to the VFRoe-ncv scheme without GRU step. The red and blue curves correspond respectively to test case A and test case B. The meshes contain from 10 to 100000 cells.

3.3 A single-phase test case involving the pathological behavior

The pathological behavior highlighted in section 2.2.3 is clearly a weakness of the GRU step. In this section the method is assessed on a test case that is prone to this behavior. Indeed, the previous test cases are based on initial conditions for ϕ which consists in Heaviside functions. In fact, the latter ensure that the front is very unlikely to disappear. Therefore, the single-phase problem of section 3.1 with the high-speed contact wave is

slightly modified. The initial conditions for density, velocity and pressure are kept as depicted in table 2, while for the scalar quantity we set:

$$\phi(t=0,x) = \begin{cases} 1, & \text{if} \quad |x - 1/2| < 0.01, \\ 0, & \text{otherwise.} \end{cases} \tag{16}$$

It should be noticed that the problem associated with these initial conditions is no more a classical Riemann problem. Though, the analytical solution may be computed. Indeed since variables (ρ, U, P) do not depend on ϕ, they are associated with a Riemann sub-problem that can thus be solved in a classical manner. Once the solution of the latter has been obtained, ϕ can be solved by integrating the advection equation with a known velocity field. Nevertheless, in this section we do not need to compute this exact solution.

Indeed, we intend to focus here on the conservation property for $\rho\phi$. We define the quantity $\mathcal{R}(t)$ as:

$$\mathcal{R}(t) = \int_{[0,1]} (\rho\phi)(t,s)ds.$$

Then, first equation of (3.2) is integrated over $[0,1]$ and it leads to:

$$\partial_t\left(\mathcal{R}\right) + (\rho U \phi)(t,1) - (\rho U \phi)(t,0) = 0. \tag{17}$$

With the final time t_{max} chosen here, the VNL waves have not yet reached the boundaries of the domain so that the velocity field remains equal to zero on the boundaries of the domain for all $t < t_{max}$. Thus, we get from relation (17) that $\mathcal{R}$ is a constant for $t < t_{max}$:

$$\forall t < t_{max}, \quad \mathcal{R}(t) = \mathcal{R}(0).$$

The initial condition for ϕ is a rectangular function centered on $1/2$ and of width 0.02, and with the initial values of table 2 we obtain: $\mathcal{R}(0) = 0.02 \times (\rho_R + \rho_L)/2 \sim 0.012654141$. When computing an approximate solution with the GRU step, and when the pathological behavior occurs, the two following situations are possible: ϕ is equal to zero in all the cells or ϕ is equal to 1 in all the cells. Considering the present initial conditions, the former situations lead to $\mathcal{R} = 0$ and the latter situations lead to $\mathcal{R} = (\rho_R + \rho_L)/2 \sim 0,63270705$.

Approximated solutions for the problem described here are then computed with the GRU step for different mesh sizes and for different couples (K_1, K_2). A wide range of couples (K_1, K_2) has been used while restricting to relatively coarse meshes. Indeed, to diminish the statistical noise the parameters of the sequences have been chosen in $\mathcal{P}(39) \times \mathcal{P}(39)$ and with $K2 < K_1$ (see section 2.4). This gives 741 different Halton-Van der Corput sequences. Obviously, when considering the computational domain $[0,1]$ and uniform meshes, at least 51 cells are needed to get a correct approximated initial condition. However, in order to ensure that the approximated initial fronts coincide with the exact initial front, we only consider in the following numbers of cells of the form $100 \times k$, with $k > 0$ an integer.

In figure 9 three quantities have been plotted:

- $\mathcal{R}(t_{max})$ is plotted for each computation (i.e. for each mesh size and each couple (K_1, K_2));

- the average quantity $< \mathcal{R}(t_{max}) >$ obtained by summing $\mathcal{R}(t_{max})$ for a given mesh size over all the couples (K_1, K_2);

- the value $\mathcal{R}(0) = 0.012654141$.

Two important remarks can be done. First, the pathological behavior occurs here for the meshes up to 400 cells. This tends to show that mesh refinement (for a given final time and a given CFL) allows to diminish the probability of occurrence of the pathological behavior. Moreover, for this test case it can be observed that the GRU step is conservative in a statistical sense. Even if the number of realizations (i.e. 741 for each mesh size) is not large enough, we can observe that the average of $\mathcal{R}(t_{max})$ tends to $\mathcal{R}(0)$. It seems that the number of realizations needed to obtain a satisfactory statistical convergence depends on the mesh size.
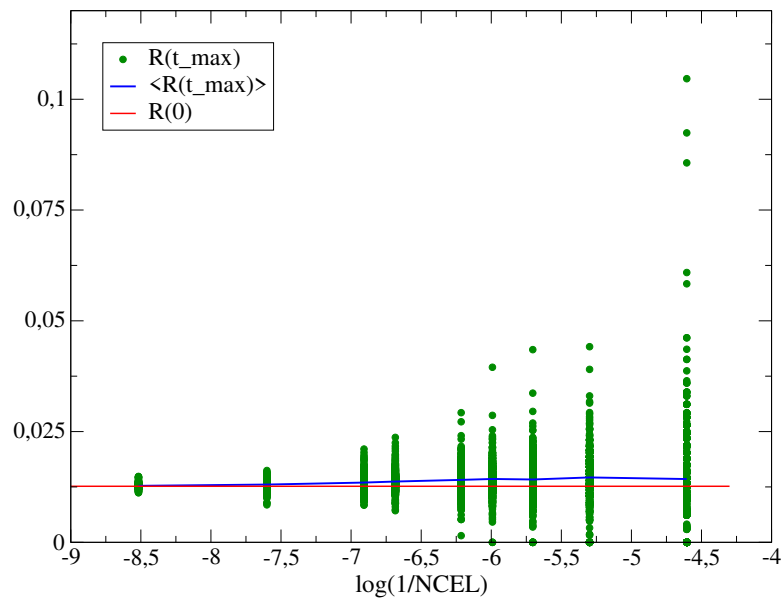
Figure 9: Convergence curves for the quantity $\mathcal{R}(t_{max})$ with respect to the mesh size. Each green point corresponds to one realization (there are 741 realizations for each mesh size, but some many coincide). The blue line corresponds to the quantity $\mathcal{R}(t_{max})$ averaged over the couples (K_1, K_2). The red line corresponds to the exact solution $\mathcal{R}(0)$. The meshes contain from 100 to 5000 cells.

4 Extension to multi-dimensional problems

As mentioned earlier in this paper, we are interested in simulating front propagation in multidimensional domains discretized with unstructured meshes. Without any loss of generality, we focus here on the two-dimensional case. The system of equations thus corresponds to the two-dimensional counterpart of system (2), that is:

$$\left\{ \begin{array}{l} \partial_t \left(\rho \right) + \partial_x \left(\rho U_x \right) + \partial_y \left(\rho U_y \right) = 0, \\ \partial_t \left(\rho \phi \right) + \partial_x \left(\rho U_x \phi \right) + \partial_y \left(\rho U_y \phi \right) = 0, \end{array} \right. \tag{18}$$

where U_x and U_y denotes respectively the velocity component along the x and y axis. As for section 2, the density ρ and the velocity field (U_x, U_y) are given.

For this kind of applications it is known that the Glimm scheme provides good results on structured meshes when using an alternate direction fractional step approach [16]. Nevertheless, the Glimm scheme can not be extended to unstructured meshes. In this section, we propose to test the GRU step on several two-dimensional problems. First, In section 4.1 we use the mono-dimensional analytical solution of section 6.2 as a test case of front propagation on unstructured meshes. Then, in section 4.2 we consider the solid rotation of a square and of a Zalesak's "C" shape [22] on structured meshes. At last, a non-solid rotation of a non-convex shape is investigated in section 4.3 considering both structured and unstructured meshes. For each test case, the analytical solutions are known and convergence curves are computed in terms of the logarithm of the L^1-error with respect to the logarithm of the mesh size. The computational domain for the test cases presented above is the square $[0,1] \times [0,1]$ and the meshes are all based on structured meshes containing $N \times N$ square cells, hence the mesh size considered is $1/N$.

Two different schemes are tested: the Upwind scheme and the Upwind-GRU scheme. The GRU step is exactly the same than for one-dimensional setting (9). It should be emphasized that the GRU step is mandatory only for the cells that neighbors the front at the beginning of the time-step. It is not necessary to perform the update on all the cells of the computational domain.

For the following two-dimensional test cases, the $(17, K2)$ Halton-Van der Corput sequences have been excluded from the studies. They appear to give very bad results. The choice of the sequence seems more crucial for the two-dimensional framework than for the one-dimensional one. In section 4.4 some observations are provided concerning the influence of the choice of the sequence on the results.

At last, it should be mentioned that, in this section, the computations on the finest meshes have been performed on several processors. Indeed, the GRU step corresponds to a cell-located update and thus no adaptation is required for multi-processor computations.

4.1 Propagation of a planar front on unstructured meshes

For this first test case, we study the ability of the Upwind-GRU scheme to propagate a planar front on unstructured meshes. We thus consider here the solution proposed in section 6.2 and already used in section 2. We thus choose: $U_y(t,x,y) = 0$ and $U_x(t,x,y) = U(t,x)$, where $U(t,x)$ is given by formula (29), and $\rho(t,x,y) = \rho(t,x)$, where $\rho(t,x)$ is given by (27). The initial condition for the scalar ϕ is:

$$\phi(t,x,y) = \left\{ \begin{array}{ll} 1, & \text{if } x < 0.1, \\ 0, & \text{otherwise.} \end{array} \right. \tag{19}$$

With the parameters $x_0 = 0.3$, $U_0 = 2$, $R_0 = 2$ and $B_0 = -1$, the solution proposed in section 6.2 corresponds at time $t_{end} = 0.58$ to a planar front located $x_{end} = 0.90305030355$:

$$\phi(t_{end}, x, y) = \left\{ \begin{array}{ll} 1, & \text{if } x < x_{end}, \\ 0, & \text{otherwise.} \end{array} \right. \tag{20}$$

In order to assess the accuracy of the schemes, numerical approximations of the solution described above are computed on unstructured meshes. These meshes are built on the basis of structured meshes with $N \times N$ square cells. Then some nodes are modified, in order to "twist" the cells around the center $(0.5, 0.5)$ of the square. The transformation of the nodes is based on the polar coordinates centered on the center of the domain $[0,1] \times [0,1]$. We set:

$$r(x,y) = \sqrt{(x-0.5)^2 + (y-0.5)^2}, \quad \text{and, if } r \neq 0, \ (r_x(x,y), r_y(x,y)) = \left(\frac{0.5 - y}{r}, \frac{x - 0.5}{r} \right)$$

and the transformation (X_p', Y_p') of coordinates (X_p, Y_p) of the nodes p is:

$$\begin{cases} X_p' = X_p + r_x(X_p, Y_p)\ D_0\ e^{-(\delta r)^2}, \\ Y_p' = Y_p + r_y(X_p, Y_p)\ D_0\ e^{-(\delta r)^2}, \end{cases} \tag{21}$$

where $D_0 = 0.08$ and $\delta r = (r(X_p, Y_p) - R_0)/\sigma$, with $R_0 = 0.2$ and $\sigma = 0.06$. Examples of such meshes are shown in figure 10.

The approximated solutions obtained with or without the GRU step are presented in figure 11 for several meshes and for the $(5, 3)$ Halton-Van der Corput sequence. It can be observed that the part of the front that travels across the twisted zone of the meshes is less accurately approximated than the upper and lower parts of the front. On the finest mesh that contains 1500×1500 cells, the approximated solution differs from the exact one on only four cells. When considering the average L^1-error between the approximated solutions and the analytical solution, it can be seen that the GRU step improves the accuracy on coarse meshes. Moreover, the convergence rate with the GRU step is equal to 0.8 whereas the Upwind scheme (without the GRU step) quickly reaches its asymptotic convergence rate of $1/2$.
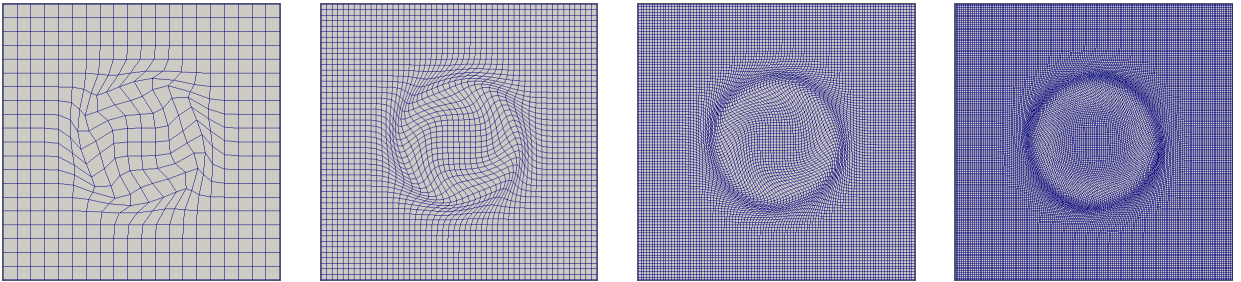

Figure 10: Examples of unstructured "twisted" meshes used for the front propagation test case: 20×20 cells, 50×50 cells, 100×100 cells and 150×150 cells.

4.2   Solid rotation of shapes on structured meshes

A classical class of problems for assessing scalar transport algorithms consists in simulating the solid rotation of shapes on structured meshes. We consider here meshes composed of $N \times N$ squared cells. and we investigate two test cases by considering the solid rotation around the center $(0.5, 0.5)$ of the computational domain $[0, 1] \times [0, 1]$. The analytical solution for the density is $\rho(t, x, y) = 1.0$ and for the velocity $U_x(t, x, y) = \theta_0(0.5 - y)$ and $U_y(t, x, y) = \theta_0(x - 0.5)$, where $\theta_0 = 1$. With these choices, the initial profile for ϕ rotates around the point $(0.5, 0.5)$. We consider the final solution at time $t_{end} = 2\Pi$, so that the initial profile for ϕ has achieved a complete rotation, and thus we have $\phi(0, x, y) = \phi(t_{end}, x, y)$. Two initial profiles are considered here. We have $\phi(0, x, y) = 0$ everywhere, except on the following considered shapes:

- for the square we have $\phi(0, x, y) = 1$ for $0.4 \leq x \leq 0.6$ and $0.65 \leq y \leq 0.85$;

- for the Zalesak's "C" shape, based on the solution proposed in [22], we have $\phi(0, x, y) = 1$ if $(x - 0.5)^2 + (y - 0.75)^2 \leq (0.15)^2$ and $(x, y) \notin \{y < 0.8$ and $0.45 < x < 0.55\}$

The second shape is non-convex as shown on the third line of figures in figure 15. Figure 13 and figure 15 respectively present the results obtained with and without the GRU step for the square test case and for the Zalesak's "C" shape.

It can be observed on the convergence curves in figures 14 and 16 that the Upwind scheme reaches its asymptotic rate of convergence 0.5 only for the finest meshes when considering the non-convex shape test-case, whereas it recovers the convergence rate 0.5 on coarser meshes for the square test case. On the contrary, the Upwind-GRU scheme presents almost the same convergence behavior for both test cases. Moreover, the GRU step improves the accuracy of the approximated solutions and its convergence rate is close to 0.8. On the coarsest meshes, the GRU step may loose the non-convex shape of the Zalesak's "C" shape. This is due to the pathological behavior illustrated by figure 1b of section 2.2. On really coarse meshes, this might even lead to the disappearance of the shape or a part of the shape. Such a behavior is highlighted by the third test case, in the next section.
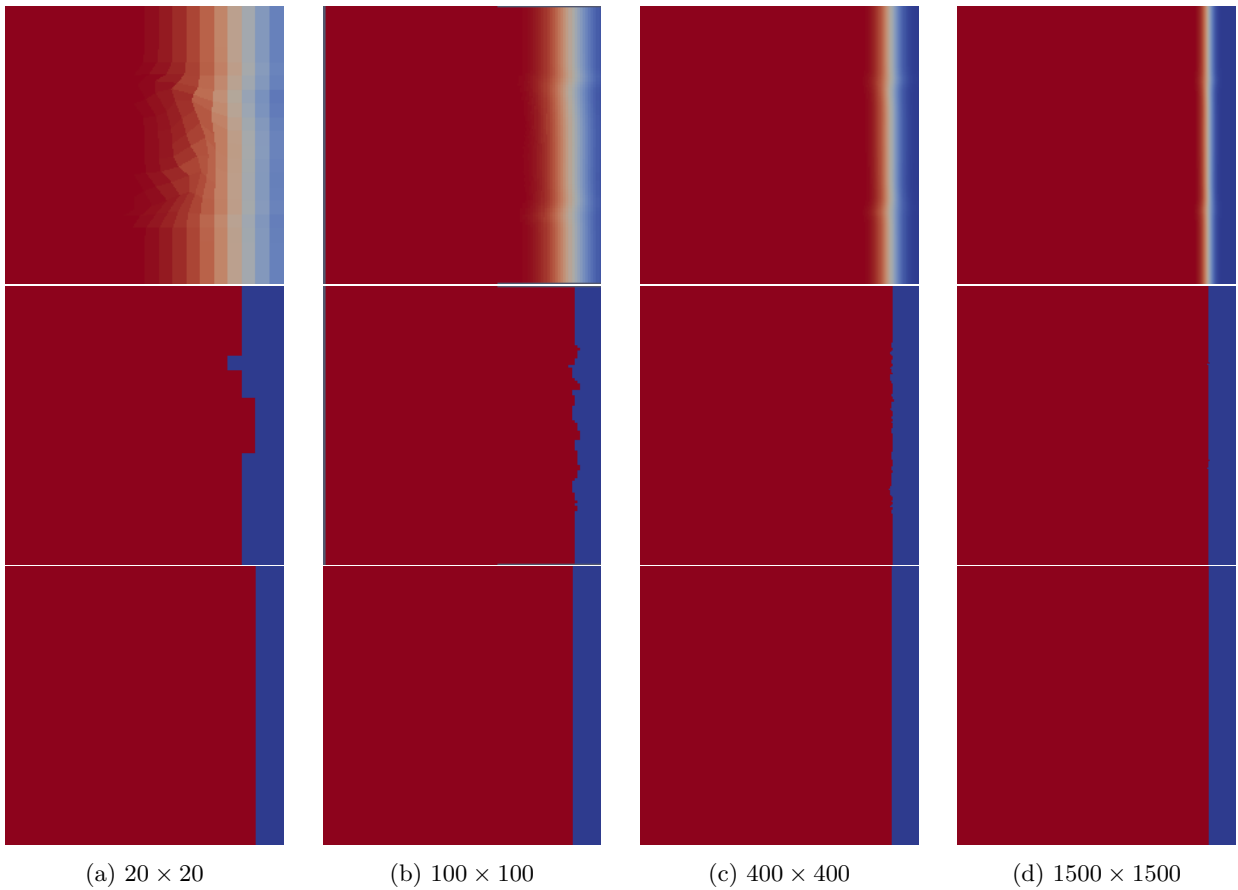
(a) 20×20 (b) 100×100 (c) 400×400 (d) 1500×1500

Figure 11: Propagation of a planar front on unstructured meshes, results obtained with the $(5, 3)$ Halton-Van der Corput sequence. First row: Upwind scheme, second row: Upwind-GRU scheme and third row: exact final shape. First column: 20×20 cells, second column: 100×100 cells, third column: 400×400 cells and forth column: 1500×1500 cells.
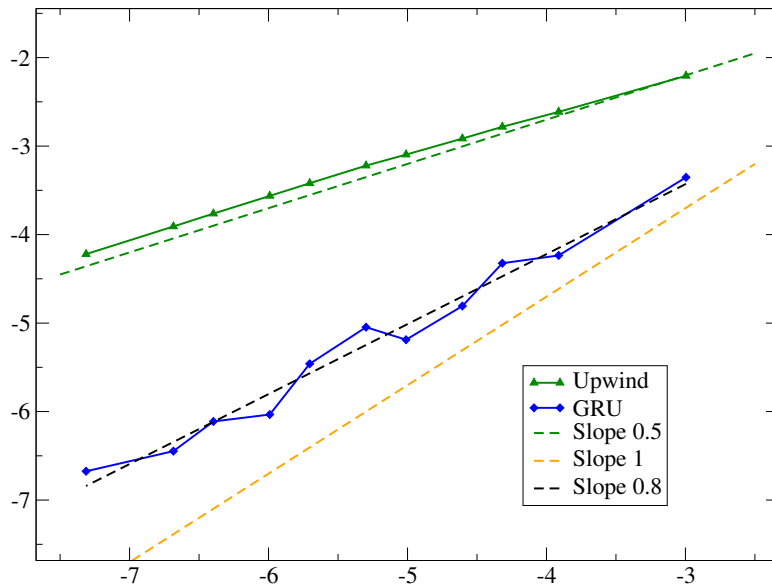
Figure 12: Convergence curves for the propagation of a front on an unstructured mesh. The green line represents the results for the sole Upwind scheme, whereas the blue line stands for the Upwind-GRU scheme.

4.3   Non-solid rotation of non-convex shapes on structured and unstructured meshes

It has been seen in the previous section that the pathological behavior described by figure 1b of section 2.2 might lead to the disappearance of the shape, or of a part of the shape. Indeed, when the latter possesses a
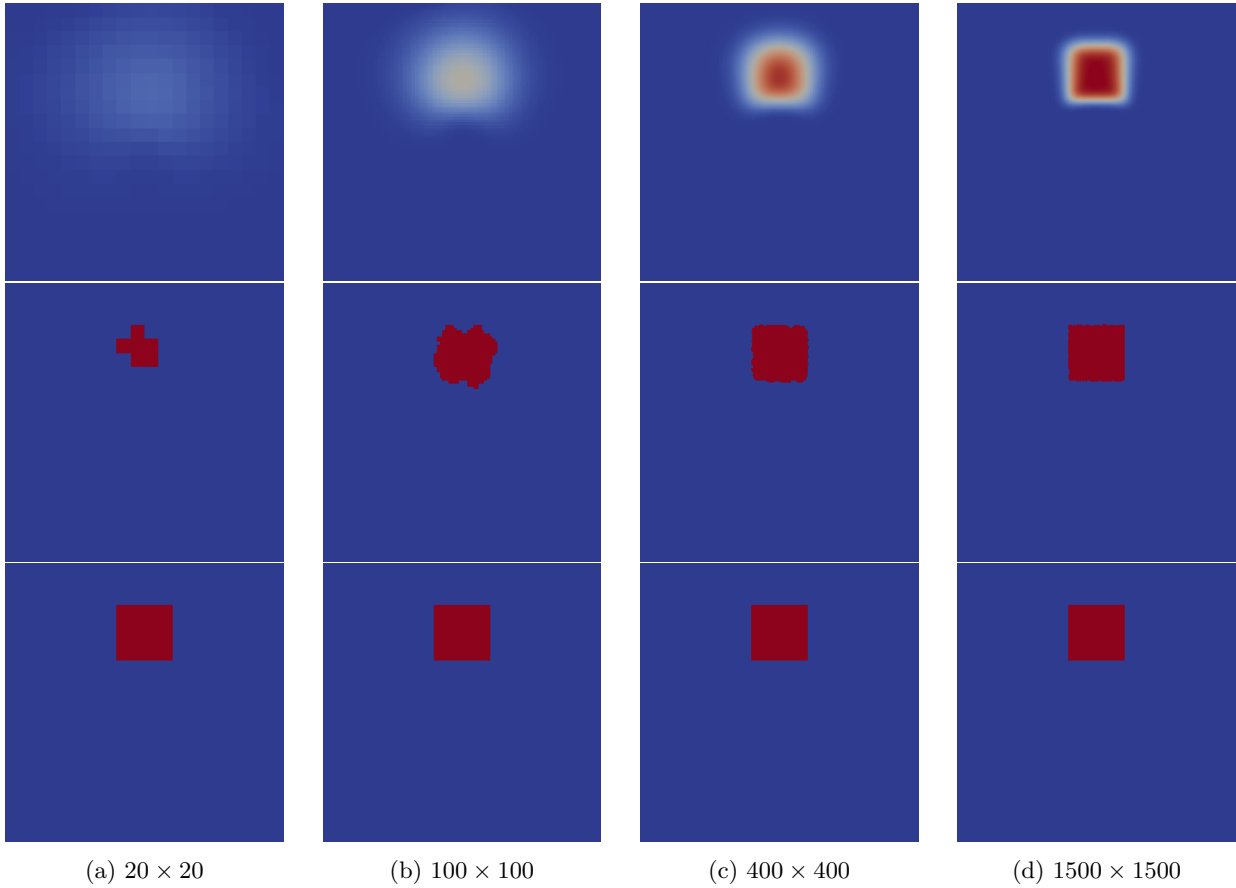
(a) 20 × 20   (b) 100 × 100   (c) 400 × 400   (d) 1500 × 1500

Figure 13: Rotation of a square on structured meshes, results obtained after one complete rotation with the (5, 3) Halton-Van der Corput sequence. First row: Upwind scheme, second row: Upwind-GRU scheme and third row: exact initial and final shape. First column: 20 × 20 cells, second column: 100 × 100 cells, third column: 400 × 400 cells and forth column: 1500 × 1500 cells.
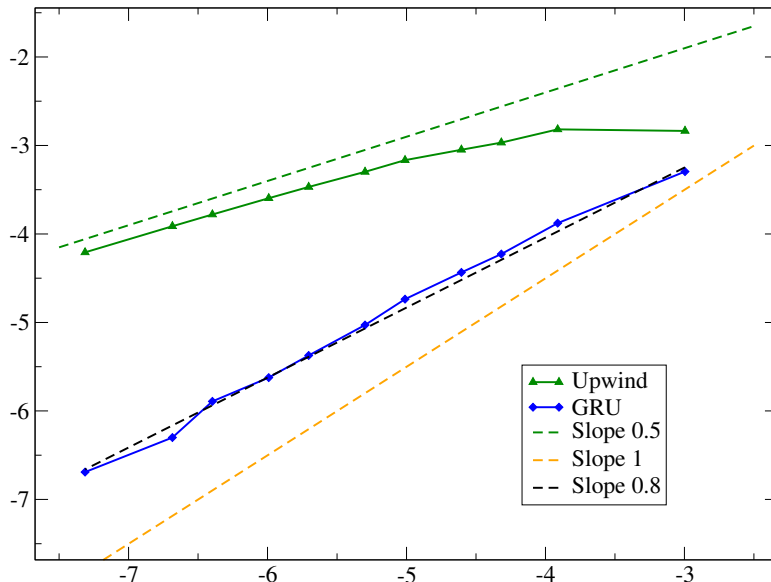
Figure 14: Convergence curves for the rotation of a square on a structured mesh. The green line represents the results for the sole Upwind scheme, whereas the blue line stands for the Upwind-GRU scheme.

two-cell wide part, it may be "erased" by the GRU step. In order to illustrate this behavior, we consider here a non-solid rotation of the Zalesak's "C" shape of the previous section. We thus consider the velocity field:

$$U_x(t, x, y) = a \ r \ \theta_0 (0.5 - y) \quad \text{and} \quad U_y(t, x, y) = a \ r \ \theta_0 (x - 0.5),$$

where $r > 0$ is the distance to the center of the domain, $r^2 = (x - 0.5)^2 + (y - 0.5)^2$, and $\theta_0 = 1$. The parameter a allows to inverse the direction of the rotation at the half of the simulation time t_{end}: $a = 1$ if $t < t_{end}/2$ and $a = -1$ if $t_{end}/2 \leq t \leq t_{end}$. The density is uniform $\rho(t, x, y) = 1$. Hence the initial shape is expanded until $t_{end}/2$ and then it is collapsed to its initial shape. The analytical solution at t_{end} is thus known for the scalar ϕ since as for the test cases of the previous section we have $\phi(0, x, y) = \phi(t_{end}, x, y)$. We choose here $t_{end} = 6\Pi$, so that the shape approximatively makes the half of a rotation before going back to its initial position. In figure 18 the approximated solutions obtained for the structured mesh with 1500×1500 cells are plotted.

During the first half of the rotation, the shape is stretched and thin parts appear, see for instance figure 18. On coarse meshes this thin parts may undergo the pathological issue described in section 2.2, and some area of the shape may be erased by the GRU step. Hence the shape may be split into several parts. If one of these parts becomes too small, it might disappear. Such a case is illustrated by figure 17 when considering a coarse mesh.

Figure 19 shows the results obtained for the final time for the Upwind scheme and for the Upwind-GRU scheme using the $(5, 3)$ Halton-Van der Corput sequence. It can clearly be observed that the 20×20 structured mesh is too coarse for the Upwind-GRU scheme. The initial shape has almost completely disappeared, and it only remains a single red cell which does not correspond to a cell that was initially red. For this test case, the initial shape contains too few cells. In fact, it can be observed on the convergence curves of figure 20 that the structured mesh should contain at least 75×75 cells (which corresponds to the third point on the right in figure 20) in order to get a correct accuracy on the approximated solutions. Besides, it should be noted that the Upwind scheme has not yet reached its asymptotic convergence rate for the finest structured mesh with 1500×1500 cells.

In figure 21, the same test case has been considered when using the unstructured meshes described in section 4.1. The convergence curves are plotted in figure 22. For theses meshes, the Upwind scheme is not very accurate and the asymptotic rate of convergence of $1/2$ is not yet reached for the finest meshes. The results obtained with the Upwind-GRU scheme are very satisfactory, even if it seems that one should use at least a 100×100-cell mesh in order to get an significant improvement of the approximated solutions. When comparing the results on structured and unstructured meshes, the difference in terms of accuracy is more important for the Upwind-GRU scheme than for the sole Upwind scheme. Nevertheless, the loss of accuracy of the approximated solution of the Upwind-GRU scheme when turning to unstructured meshes remains reasonable.
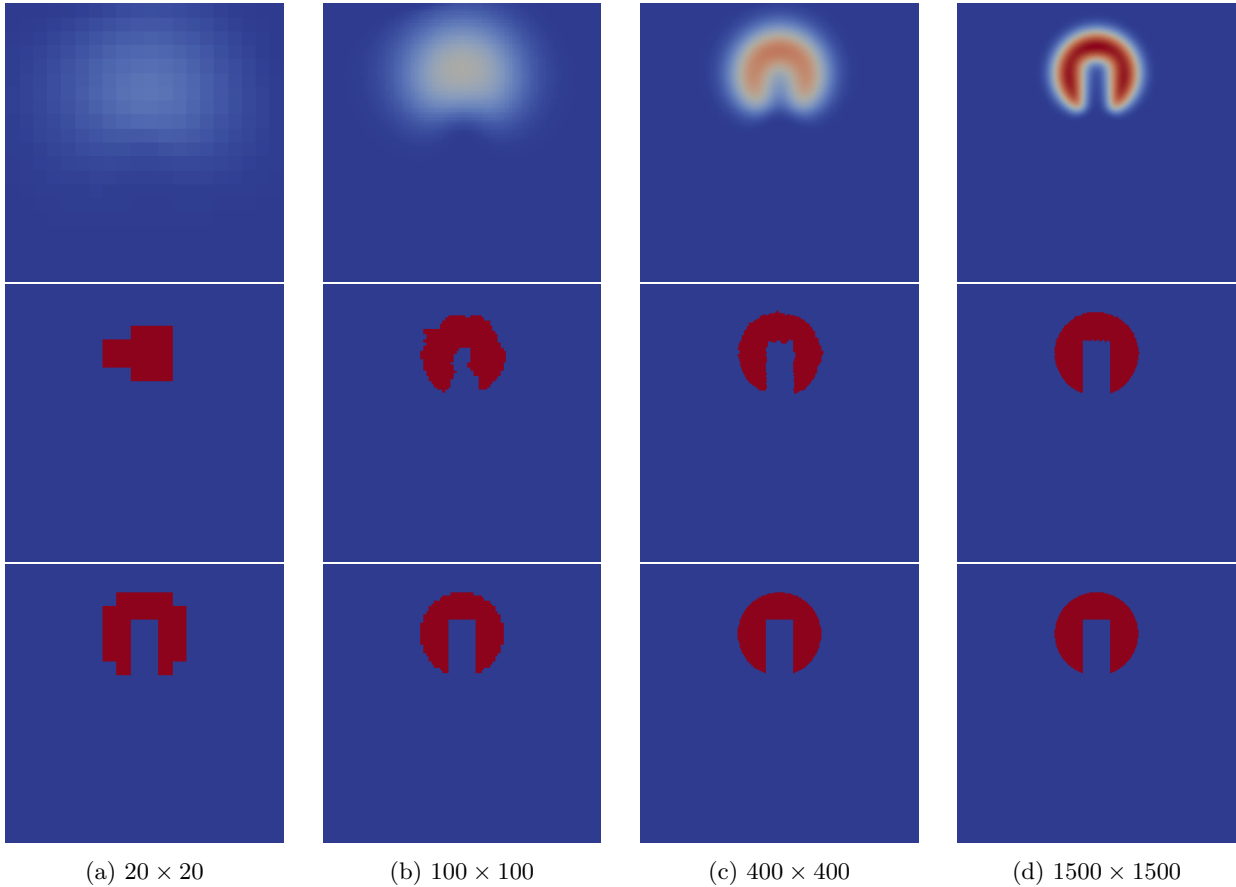
22

(a) 20×20 (b) 100×100 (c) 400×400 (d) 1500×1500

Figure 15: Rotation of the non-convex Zalesak's shape on structured meshes, results obtained after one complete rotation with the $(5, 3)$ Halton-Van der Corput sequence. First row: Upwind scheme, second row: Upwind-GRU scheme and third row: exact initial and final shape. First column: 20×20 cells, second column: 100×100 cells, third column: 400×400 cells and forth column: 1500×1500 cells.
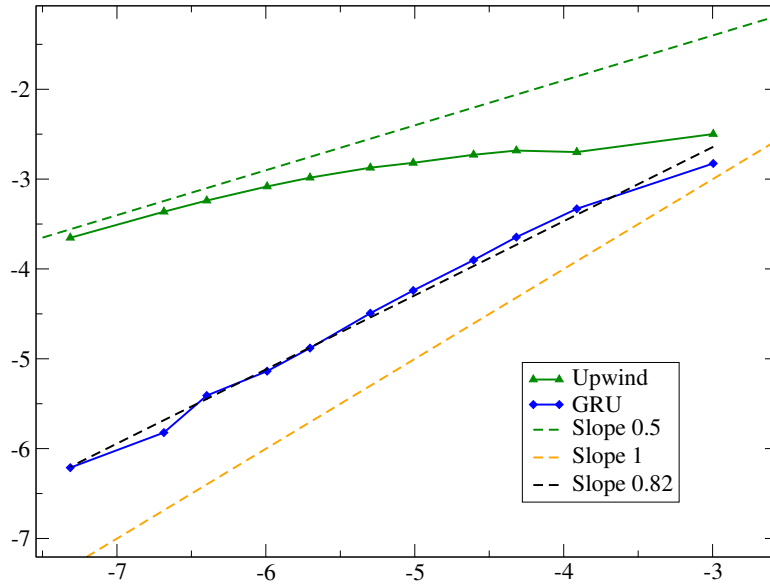
Figure 16: Convergence curves for the rotation of the non-convex Zalesak's shape on a structured mesh. The green line represents the results for the sole Upwind scheme, whereas the blue line stands for the Upwind-GRU scheme.
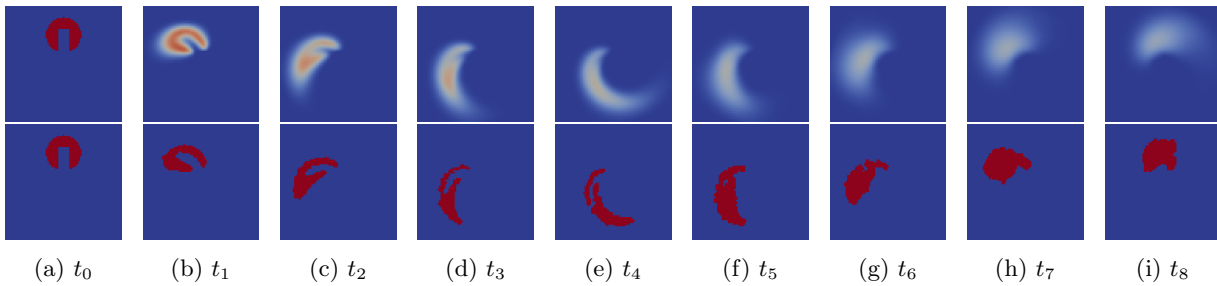

(a) t_0 (b) t_1 (c) t_2 (d) t_3 (e) t_4 (f) t_5 (g) t_6 (h) t_7 (i) t_8

Figure 17: Non-solid rotation of the Zalesak's "C" shape for the structured mesh containing 75×75 cells at different times $t_i = i \times 6\Pi/8$. Time t_8 corresponds to the final time of the simulation at which the analytical solution corresponds to the figure for t_0. The computations have been performed here with the $(23, 5)$ Halton-Van der Corput sequence. First row: approximated solutions for the Upwind scheme, second row: approximated solutions for the Upwind-GRU scheme. It can be seen in figure (d) that the upper arm of the shape is refined to a few cells. In figure (e), this arm has been separated from the rest of the shape by the GRU step. Then, the two arms are collapsed and a "blue hole" appears in figure (f). Because of its thinness, this hole might also have been erased by the GRU step.
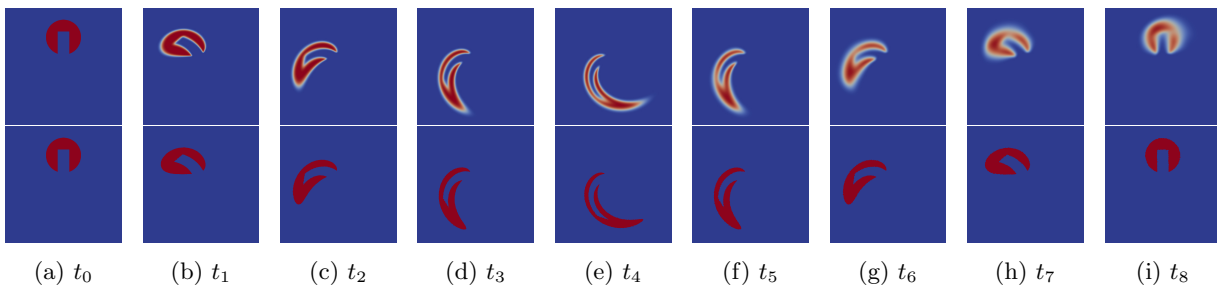

(a) t_0 (b) t_1 (c) t_2 (d) t_3 (e) t_4 (f) t_5 (g) t_6 (h) t_7 (i) t_8

Figure 18: Non-solid rotation of the Zalesak's "C" shape for the structured mesh containing 1500×1500 cells at different times $t_i = i \times 6\Pi/8$. Time t_8 corresponds to the final time of the simulation at which the analytical solution corresponds to the figure for t_0. The computations have been performed here with the $(5, 3)$ Halton-Van der Corput sequence. First row: approximated solutions for the Upwind scheme, second row: approximated solutions for the Upwind-GRU scheme.
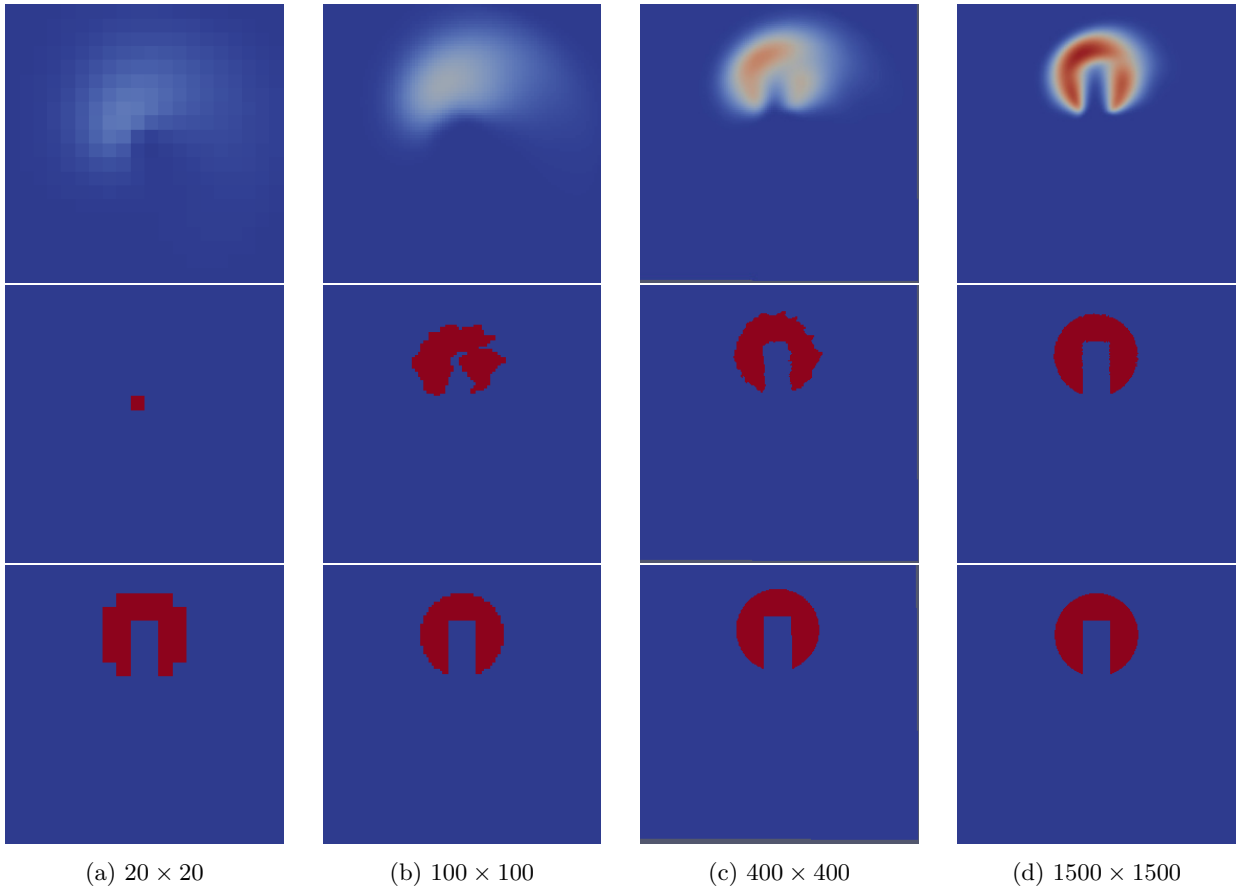
24

Figure 19: Non-solid rotation of the non-convex Zalesak's shape on structured meshes, results obtained after one complete rotation with the $(5,3)$ Halton-Van der Corput sequence. First row: Upwind scheme, second row: Upwind-GRU scheme and third row: exact initial and final shape. First column: 20×20 cells, second column: 100×100 cells, third column: 400×400 cells and forth column: 1500×1500 cells.
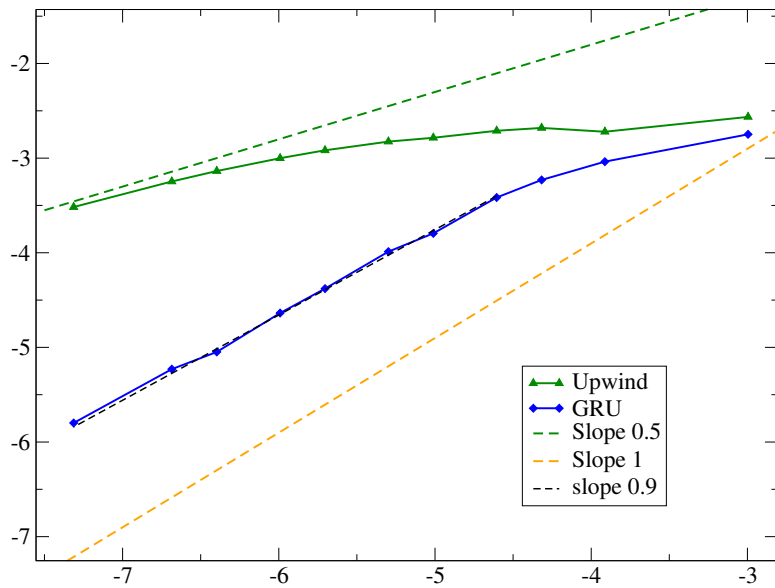

Figure 20: Convergence curves for the non-solid rotation of the non-convex Zalesak's shape on structured mesh. The green line represents the results for the sole Upwind scheme, whereas the blue line stands for the Upwind-GRU scheme.
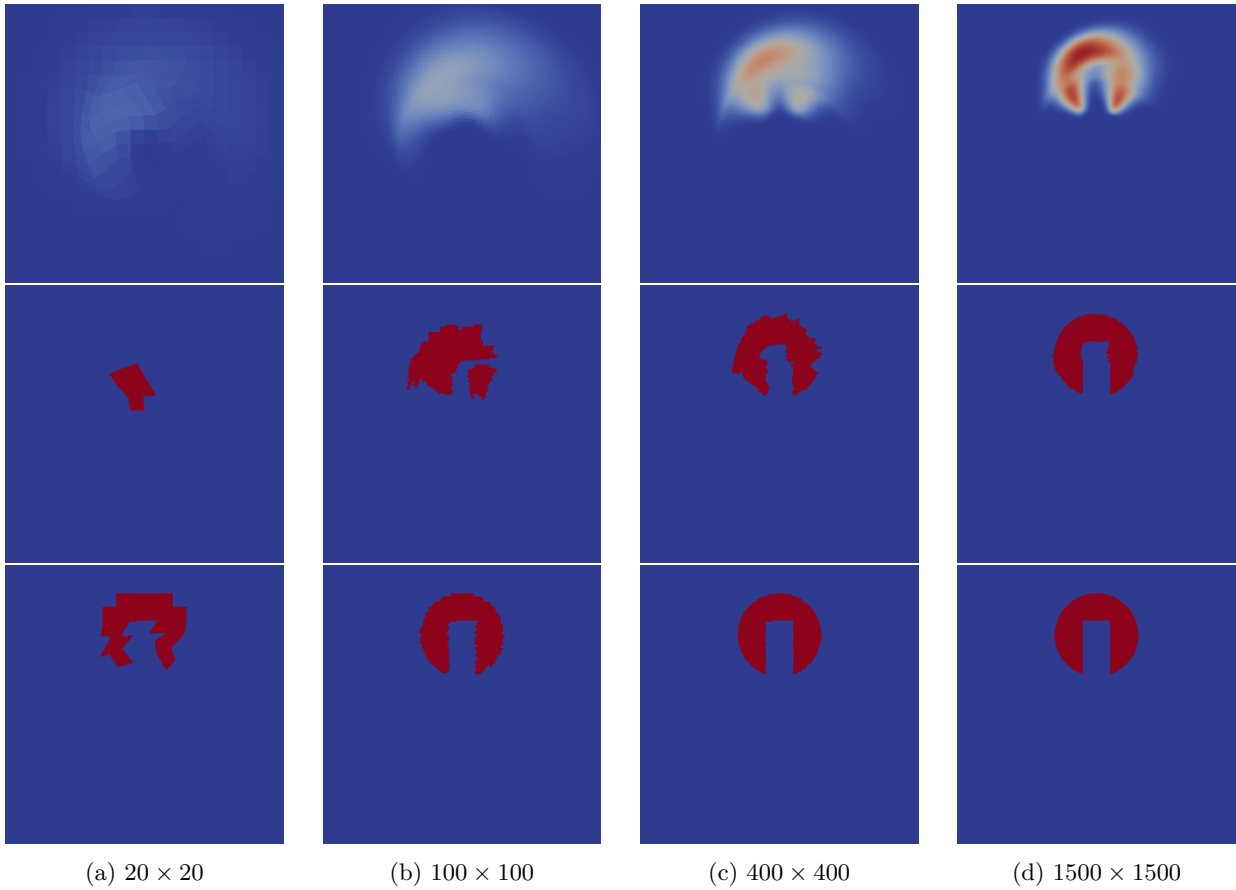
(a) 20×20 (b) 100×100 (c) 400×400 (d) 1500×1500

Figure 21: Non-solid rotation of the non-convex Zalesak's shape on unstructured meshes, results obtained after one complete rotation with the $(5, 3)$ Halton-Van der Corput sequence. First row: Upwind scheme, second row: Upwind-GRU scheme and third row: exact initial and final shape. First column: 20×20 cells, second column: 100×100 cells, third column: 400×400 cells and forth column: 1500×1500 cells.
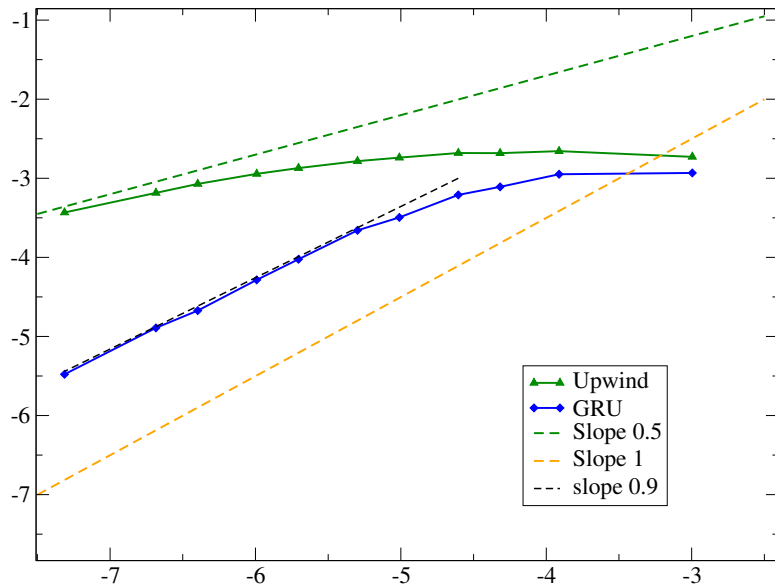

Figure 22: Convergence curves for the non-solid rotation of the non-convex Zalesak's shape on unstructured meshes. The green line represents the results for the sole Upwind scheme, whereas the blue line stands for the Upwind-GRU scheme.

4.4 Discussion on the choice of the quasi-random sequence

In all the convergence studies of the previous sections, we have only considered the average convergence curves for the Upwind-GRU scheme. In a practical point of view, one can not always afford to test different sequences (because of the computational cost) and it is often impossible to know if the accuracy of the chosen sequence is good or not (because the analytical solution corresponding to the simulation is in general not known !). Hence, an important point for using the GRU step is the choice of the parameters (K_1, K_2) for the Halton-Van der Corput sequence. In this section, a short discussion on the choice of these parameters (K_1, K_2) is proposed. The remarks below obviously refer to the test cases of the previous sections with our specific choices of the sequences. A more extended and detailed study is necessary to generalize these remarks. All the convergence curves for all the couples (K_1, K_2) and all the test cases have been plotted in figures 24, 25, 26, 27 and 28.

It was already mentioned at the beginning of this section that for the two-dimensional test cases, all the sequences with $K_1 = 17$ have been excluded. Indeed, it was observed that theses sequences lead to very poor results. For all the test cases and for all the sequences used for the two-dimensional settings, the GRU step improves the L^1-error of the approximated solutions. The GRU step does not decrease the L^1-error only when using the coarsest 20×20 mesh with:

- the two sequences $(19, 11)$ and $(19, 13)$ for the test case of section 4.3 on structured meshes,

- the two sequences $(19, 11)$ and $(13, 7)$ for the test case of section 4.3 on unstructured meshes.

Nevertheless, it should be underlined that for these test cases the initial shape is only one or two cells wide. Since this thin shape is stretched, the possibility to encounter the pathological shape disappearance due to the GRU step is very important for these coarse meshes. When considering the different results obtained with the different parameters (K_1, K_2), it can be noted that the influence of the latter is important. Indeed, we can observe that for a given mesh size the error between the sequence providing the smallest error and the sequence providing the most important error is between 1 and 1.5 decades.

In figures 24, 25, 26, 27 and 28, some sequences have been highlighted. They correspond to sequences that provide numerical approximations which are either always better or always worse than the average error. It does not seem possible to extract one sequence that has a very good behavior for all meshes and all test cases. Nevertheless, it appears that some sequences always provide very good accuracy (for instance $(5, 3)$ or $(23, 5)$), and some sequences should be avoided (for instance $(23, 11)$ or $(19, 17)$).

Let us now only consider the rotation test cases of sections 4.2 and 4.3 which involve the Zalesak's "C" shape. Following the level of accuracy observed for the average convergence curves on each test case of figure 23, one could consider that: the test case of the solid rotation of the Zalesak's "C" shape on structured meshes is less complex than the test case of the non-solid rotation of the Zalesak's "C" shape on structured meshes, which is less complex than the test case of the non-solid rotation of the Zalesak's "C" shape on unstructured meshes (see figure 23 for a comparison of the average convergence curves). Assuming this order, the dispersion of the results with respect to the choice of the sequence for the Upwind-GRU scheme seems to increase when the average accuracy decreases.
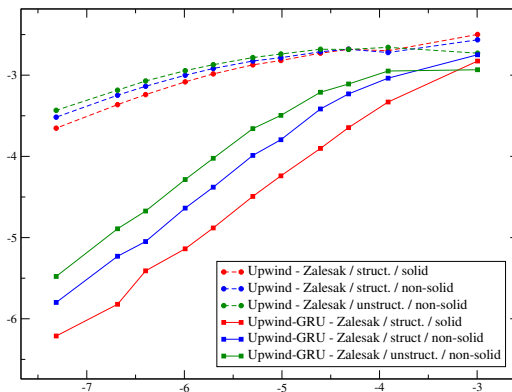

Figure 23: Comparison of the average convergence curves on the rotation test cases of the Zalesak's shape: the curves for the Upwind-GRU scheme are plotted using plain lines with squares, and the convergence curves for the Upwind scheme without the GRU step are plotted using dashed lines with circles.
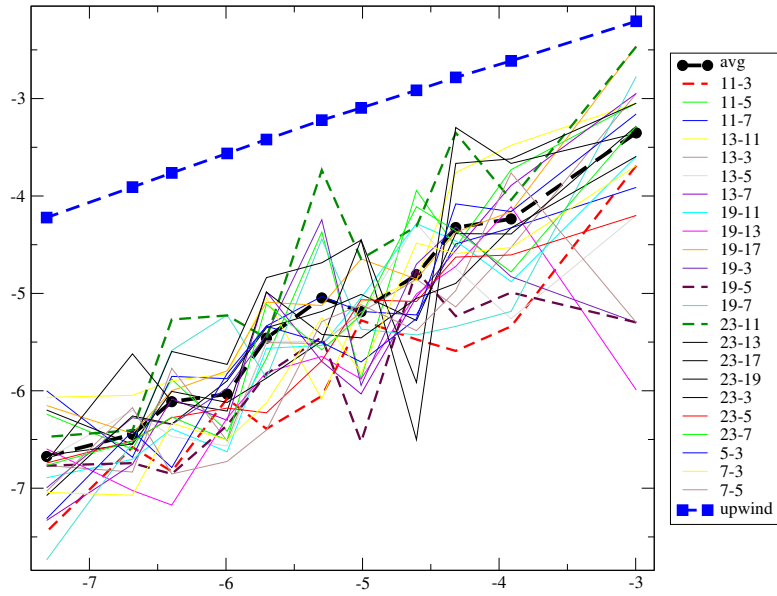
Figure 24: Upwind-GRU scheme: convergence curves for all the (K_1, K_2) Halton-Van der Corput sequences used for the front propagation test case of section 4.1. The average convergence curve is plotted in thick black dashed line with plain circles ("avg" in the legend). The convergence curve for the Upwind scheme without GRU step is plotted in thick blue dashed line with plain squares.

Figure 25: Upwind-GRU scheme: convergence curves for all the (K_1, K_2) Halton-Van der Corput sequences used for the test case of rotation of a square of section 4.2. The average convergence curve is plotted in thick black dashed line with plain circles ("avg" in the legend). The convergence curve for the Upwind scheme without GRU step is plotted in thick blue dashed line with plain squares.
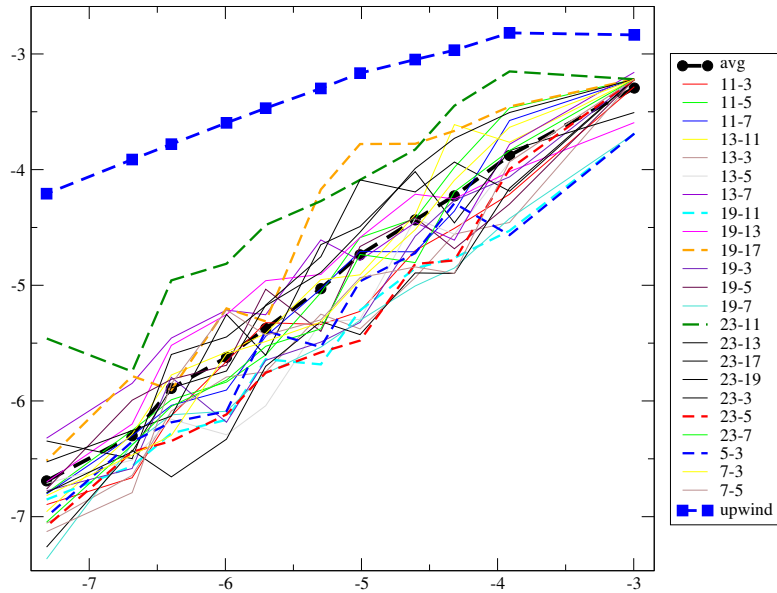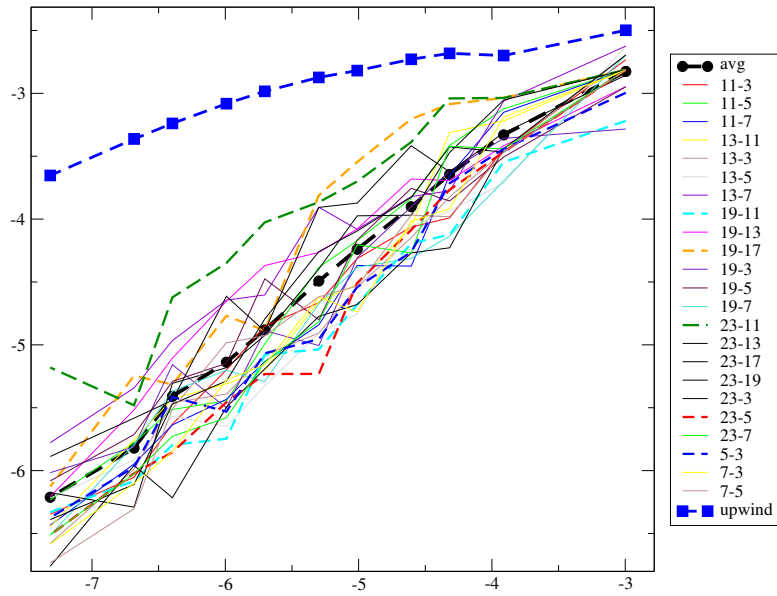
Figure 26: Upwind-GRU scheme: convergence curves for all the (K_1, K_2) Halton-Van der Corput sequences used for the test case of rotation of the Zalesak's "C" shape of section 4.2. The average convergence curve is plotted in thick black dashed line with plain circles ("avg" in the legend). The convergence curve for the Upwind scheme without GRU step is plotted in thick blue dashed line with plain squares.
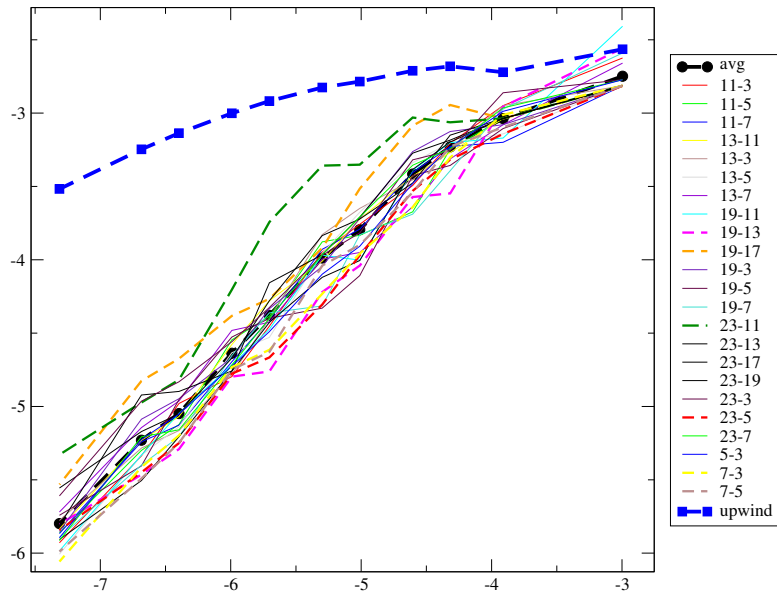
Figure 27: Upwind-GRU scheme: convergence curves for all the (K_1, K_2) Halton-Van der Corput sequences used for the test case of the non-solid rotation of the Zalesak's "C" shape on structured meshes of section 4.2. The average convergence curve is plotted in thick black dashed line with plain circles ("avg" in the legend). The convergence curve for the Upwind scheme without GRU step is plotted in thick blue dashed line with plain squares.

Figure 28: Upwind-GRU scheme: convergence curves for all the (K_1, K_2) Halton-Van der Corput sequences used for the test case of the non-solid rotation of the Zalesak's "C" shape on unstructured meshes of section 4.2. The average convergence curve is plotted in thick black dashed line with plain circles ("avg" in the legend). The convergence curve for the Upwind scheme without GRU step is plotted in thick blue dashed line with plain squares.
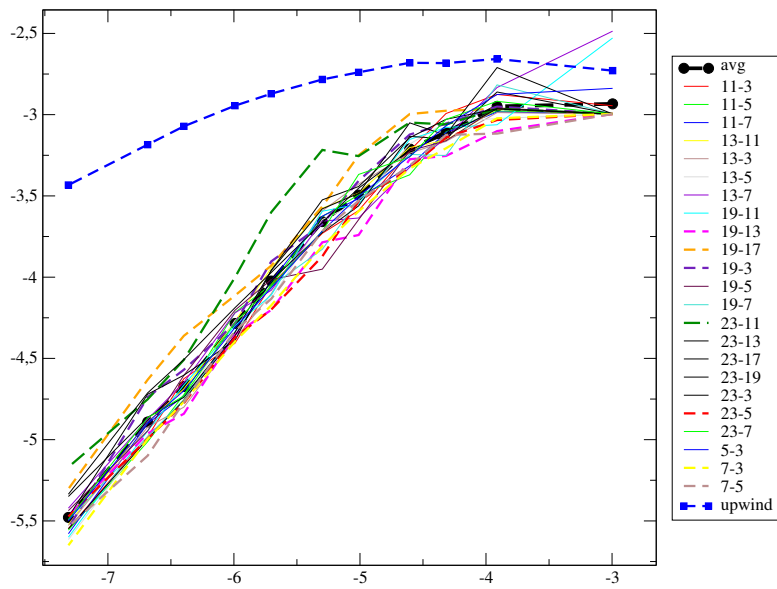
5 Conclusion

The GRU step proposed in the sequel has been tested on one-dimensional and two-dimensional test cases of front propagations, included unstructured meshes. It is based on the idea of the Glimm's method [13] in the sense that it's compressive behavior arises from a random choice. Even if more accurate and efficient methods exist for front tracking, this GRU step draws its strength from its extreme simplicity of implementation, even when considering multi-processor computations. Moreover, this projection step may be used in conjunction with a wild range of convection schemes.

The GRU step allows to get an interesting accuracy and an effective convergence rate close to 0.8 for the scalar case, and close to the convergence rate for the density when turning to the Euler case (and when considering a conservative form for the equation for ϕ). This behavior is obtained without using high order methods. It is thus easy to apply even on highly unstructured meshes. Even if it has not been widely investigated in this work (see the example in section 3.1), it is possible to implement the GRU update in conjunction with a first step build on the basis of high-order methods. The gain in terms of convergence rate would probably be limited for methods with an order less than 4. Indeed, thanks to [8], the asymptotic convergence rate for the scalar equation for ϕ is $p/(p+1)$ when using an explicit method of order p, and we have $p/(p+1) = 0.8$ for $p = 4$. Nevertheless, using high-order methods may improve the accuracy of the approximated solutions even for $1 < p \leq 4$.

Some points still need to be examined. It was shown in section 4.4 that the results are sensitive to the choice of the Halton-Van der Corput sequence. Unfortunately, no general conclusion can be drawn from the discussion of section 4.4. More extensive studies could be performed, including other choices of sequence, in order to determine if some prescriptions exist to guarantee the accuracy of the approximated solutions. Besides this, the pathological behavior pointed out in sections 2.2.3 and 3.3 is a drawback of the method, even if the numerical tests of section 4.3 tends to show that it is not critical. Actually the only parry proposed to avoid these situations is mesh refinement. Other parries may be found to make the method even more robust.

For this study, no comparison with other methods have been done. This is obviously a task to be carried out in order to situate the GRU step among the wild range of the methods proposed in the literature: high-order methods, anti-diffusive schemes, VOF methods, level-set methods, VOFIRE scheme, etc ... At last, some theoretical results about the behavior of the GRU step should be derived in order to confirm (or not) the results that have been observed in the sequel for some test cases.

6 Appendices

6.1 Some properties of the Upwind scheme

We consider here the Upwind scheme defined by (7) in section 2.2. Since the latter is not classical we propose here some properties of this scheme. In this section, for the sake of readability, the following notations are used:

$$\Psi^n : x \mapsto \Psi(t^n, x) \quad \text{and} \quad \Psi_i : t \mapsto \Psi(t, (i - 1/2)\Delta x),$$

where Ψ stands for the density ρ or the velocity U. Hence we get that:

$$\Psi_i^n = \Psi(t^n, (i - 1/2)\Delta x).$$

We recall that $t^{n+1} = t^n + \Delta t$. It is assumed that the time step fulfills the CFL constraint (4). We examine in the following if some additional constraints have to be fulfilled in order to guarantee the maximum principle for the scalar quantity. We also show that the Upwind scheme is TVD.

Remark. By using Taylor expansions with respect to x for the mass fluxes $Q_{i+1/2}^n = (\rho U)_{i+1/2}^n$ and a Taylor expansion with respect to t for the density ρ_i^{n+1}, and by assuming that Δt and Δx are linked through a CFL condition, one can easily obtain from the mass equation of (7) that:

$$\rho_i^{n+1,*} = \rho_i^{n+1} - \frac{(\Delta t)^2}{2}(\partial_{tt}\rho)_i^n + o((\Delta t)^2).$$

Mass equation
The mass equation of (7) gives at time t^n:

$$(\partial_t (\rho))^n + (\partial_x (\rho U))^n = 0.$$

By integrating this equation over the cell i, we obtain thanks to the Green formula:

$$\int_{[(i-1)\Delta x, i\Delta x]} (\partial_t (\rho))^n = -(Q_{i+1/2}^n - Q_{i-1/2}^n) = \frac{\Delta x}{\Delta t}(\rho_i^{n+1,*} - \rho_i^n).$$

Hence, the mass $\rho_i^{n+1,*}$ is non-negative if and only if:

$$\rho_i^n + \frac{\Delta t}{\Delta x} \int_{[(i-1)\Delta x, i\Delta x]} (\partial_t (\rho))^n > 0. \tag{22}$$

From equation (22) an explicit constraint on Δt can be deduced in order to ensures the positivity of $\rho_i^{n+1,*}$ for all cells i. It should be noted that for constant densities, as it is the case in section 4 (except for the first test case), no additional constraint arises from (22). When considering the analytical solutions of section (6.2) and (6.3), relation (22) gives thanks to the density (27):

$$1 + \frac{\Delta t}{\Delta x}B_0 \left(e^{R_0\Delta x/2} - e^{-R_0\Delta x/2}\right) > 0.$$

Thus, considering the choices $R_0 > 0$ and $B_0 < 0$, the relation above can be written:

$$\Delta t < \frac{\Delta x}{|B_0 \left(e^{R_0\Delta x/2} - e^{-R_0\Delta x/2}\right)|}.$$

Yet, for these parameters the constraint (4) gives: $\Delta t < \Delta x/4$. Since for all Δx in $[0, 1]$, $\left(e^{R_0\Delta x/2} - e^{-R_0\Delta x/2}\right) < 4$, the constraint (4) leads to a smaller time step Δt than the constraint (22) when considering the solutions of sections (6.2) and (6.3).

In other words, for the test cases of sections 2 and 6.4 and for the first test case of section 4, $\rho_i^{n+1,*} > 0$ without any additional constraint on $\Delta t > 0$.

In the following, we assume that we are in such a case, which means that the density $\rho_i^{n+1,*} > 0$ without any additional constraint on Δt.

Transport equation for ϕ
First, it should be noted from the scheme (7) that: if $\phi_{i-1}^n = \phi_i^n = \phi_{i+1}^n$, then $\phi_i^{n+1} = \phi_i^n$ (we recall that the density is assumed to be non-negative). This property arises from the specific choice of $\rho_i^{n+1,*}$ (i.e. the second equation of (7)). For the general setting, we distinguish four cases for the update of the discrete scalar value in the cell i.

- **Case 1:** $Q_{i-1/2}^n > 0$ **and** $Q_{i+1/2}^n > 0$.
  We have:
  $$\phi_i^{n+1,*} = \left(1 - \frac{\Delta t}{\Delta x}\frac{Q_{i-1/2}^n}{\rho_i^{n+1,*}}\right)\phi_i^n + \left(\frac{\Delta t}{\Delta x}\frac{Q_{i-1/2}^n}{\rho_i^{n+1,*}}\right)\phi_{i-1}^n.$$

- **Case 2:** $Q_{i-1/2}^n \le 0$ **and** $Q_{i+1/2}^n > 0$.
  We have:
  $$\phi_i^{n+1,*} = \phi_i^n.$$

- **Case 3:** $Q_{i-1/2}^n > 0$ **and** $Q_{i+1/2}^n \le 0$.
  We have:
  $$\phi_i^{n+1,*} = \left(1 - \frac{\rho_i^n}{\rho_i^{n+1,*}} - \frac{\Delta t}{\Delta x}\frac{Q_{i-1/2}^n}{\rho_i^{n+1,*}}\right)\phi_{i+1}^n + \left(\frac{\rho_i^n}{\rho_i^{n+1,*}}\right)\phi_i^n + \left(\frac{\Delta t}{\Delta x}\frac{Q_{i-1/2}^n}{\rho_i^{n+1,*}}\right)\phi_{i-1}^n$$

- **Case 4:** $Q_{i-1/2}^n \le 0$ **and** $Q_{i+1/2}^n \le 0$.
  We have:
  $$\phi_i^{n+1,*} = \left(1 + \frac{\Delta t}{\Delta x}\frac{Q_{i+1/2}^n}{\rho_i^{n+1,*}}\right)\phi_i^n + \left(-\frac{\Delta t}{\Delta x}\frac{Q_{i+1/2}^n}{\rho_i^{n+1,*}}\right)\phi_{i+1}^n.$$

For the cell i, if $\Delta t > 0$ fulfills:

$$\frac{\Delta t}{\Delta x}\frac{max(|Q_{i-1/2}^n|, |Q_{i+1/2}^n|)}{\rho_i^{n+1,*}} < 1 \tag{23}$$

then update formulas for $\phi_i^{n+1,*}$ are barycentric combinations of ϕ_{i-1}^n, ϕ_i^n and ϕ_{i+1}^n for the four cases and, thus, the maximum principle for the approximated values of ϕ holds:

$$min(\phi_{i-1}^n, \phi_i^n, \phi_{i+1}^n) \le \phi_i^{n+1,*} \le max(\phi_{i-1}^n, \phi_i^n, \phi_{i+1}^n).$$

Unfortunately, the constraint (23) is implicit because of the density $\rho_i^{n+1,*}$. Assuming non-zero interfacial velocities, it can be written :

$$\Delta t < \Delta x\ \frac{\rho_i^{n+1,*}}{max(|(\rho U)_{i-1/2}^n|, |(\rho U)_{i+1/2}^n|)} \tag{24}$$

which leads to a different constraint than (4). A sufficient condition to fulfill (24) is to choose Δt such that:

$$\Delta t < \Delta x\ \frac{1}{2\ max(|U_{i-1/2}^n|, |U_{i+1/2}^n|)}\ \left(\frac{2\rho_i^{n+1,*}}{max(\rho_{i-1/2}^n, \rho_{i+1/2}^n)}\right).$$

When the density is uniform and constant, constraint (4) guarantees to fulfill (24). It should be noted that when the mesh is refined, and that the time-step follows the constraint (4), $\rho_i^{n+1,*}$ and $max(\rho_{i-1/2}^n, \rho_{i+1/2}^n)$ tend toward the same value. Hence, an additional constraint on the time step may arise from (24) on "coarse" meshes. In a practical point of view, for the test cases based on the solutions of sections 6.2 and 6.3, the constraint (4) was sufficient to guarantee the maximum principle for the approximated solutions of ϕ.

In the following we prove that under condition (23), the Upwind scheme (7) is TVD. Thanks to the results given above, the scalar quantity $\phi_i^{n+1,*}$ can be written in the form of a barycenter of the approximated values for ϕ in the neighboring cells at time t^n:

$$\phi_i^{n+1,*} = \alpha_i^n \phi_{i+1}^n + (1 - \alpha_i^n - \beta_i^n)\phi_i^n + \beta_i^n \phi_{i-1}^n,$$

where the coefficients α_i^n and β_i^n are given by the four cases above. If the time step is chosen so that for all cells i condition (23) holds, for all cells i we have $\alpha_i^n \ge 0$ and $\beta_i^n \ge 0$. We then obtain that:

$$\phi_{i+1}^{n+1,*} - \phi_i^{n+1,*} = \alpha_{i+1}^n(\phi_{i+2}^n - \phi_{i+1}^n) + (1 - \alpha_i^n - \beta_{i+1}^n)(\phi_{i+1}^n - \phi_i^n) + \beta_i^n(\phi_i^n - \phi_{i-1}^n). \tag{25}$$

When considering the four cases depicted above, we observe that for all the cells we have $\alpha_i^n \beta_{i+1}^n = 0$. Indeed, the combinations of cases (among the four cases above) for two neighboring cells i and $i+1$ that lead to $\alpha_i^n \beta_{i+1}^n \ne 0$ are not compatible with respect to sign of the mass flux $(\rho U)_{i+1/2}^n$ between these two cells. Thus, since $\alpha_i^n \ge 0$ and $\beta_{i+1}^n \ge 0$, we get that $(1 - \alpha_i^n - \beta_{i+1}^n) > 0$. As a consequence, if we assume that the sequence $\{\phi_i^n, i \in 1, N_c\}$ is monotone increasing (resp. decreasing), then the sequence $\{\phi_i^{n+1,*}, i \in 1, N_c\}$ is monotone increasing (resp. decreasing). Therefore, we deduce from the classical result given in reference[15] that the Upwind scheme (7) is TVD under the constraint (23).

6.2 A class of analytical solutions for the convection problem in conservative form

We propose here a very simple class of analytical solution for system (2) on the domain $(t, x) \in [0, T_0] \times [0, 1]$, with a bounded final time $0 < T_0$. This class of solutions possesses non-uniform but regular profiles for the density (which is non-negative) and for the velocity, and the scalar field ϕ is based on a Heaviside function. When considering regular density and velocity, the first equation of (2) can be written:

$$\partial_t (\ln(\rho)) + U \ \partial_x (\ln(\rho)) + \partial_x (U) = 0. \tag{26}$$

Since system (2) is based on two equations and three unknowns, we can specify one among this unknown. If the density ρ is chosen such that:

$$\rho(t, x) = e^{(R_0 \ (x + B_0 \ t))}, \tag{27}$$

where R_0 and B_0 are uniform and constant, then through equation (26) the velocity must fulfill:

$$\partial_x (U) + R_0 \ (U + B_0) = 0. \tag{28}$$

Equation (28) can obviously be exactly integrated on $[0, T_0] \times [0, 1]$. It yields:

$$U(t, x) = U(t, x = 0) \ e^{(-R_0 x)} - B_0 \left(1 - e^{(-R_0 x)}\right). \tag{29}$$

Let us assume that the velocity $U(t, x = 0)$ does not depend on time: $U(t, x = 0) = U_0$, so that the velocity (29) does not depend on time. We also assume that the initial profile of the scalar field is defined using a Heaviside function $\mathcal{H}(x)$:

$$\phi(t = 0, x) = \mathcal{H}(x - x_0), \tag{30}$$

with $x_0 \in]0, 1[$ and with:

$$\mathcal{H}(x) = \left\{ \begin{array}{l} 1, \ \forall x < 0; \\ 0, \ \text{otherwise}. \end{array} \right.$$

According to system (2), and since both ρ and U are regular, the solution for ϕ with initial condition (30) is an Heaviside traveling with velocity U. In order to characterize this solution, with thus have to find the location of the discontinuity. The initial discontinuity for ϕ is located at x_0. Provided that the velocity does not vanish for $t \in [0, t^*]$, this discontinuity is located at time t^* at the abscissa x^* given by the relation:

$$t^* = \int_{x_0}^{x^*} \frac{dx}{U(x)}. \tag{31}$$

It should be emphasized that relation (31) holds because the velocity does not depend on time. The velocity (29) can be written on the form: $U = b + e^{(ax)}$, and the integral in (31) can thus be exactly expressed. Indeed, we have:

$$\int_{x_1}^{x_2} \frac{dx}{b + e^{(ax)}} = \frac{-1}{ab} \ln \left(\frac{1 + be^{(-ax_2)}}{1 + be^{(-ax_1)}} \right),$$

which leads through (31) to the following expression for x^*:

$$x^* = \frac{1}{R_0} \ln \left(\left(1 + \frac{U_0}{B_0} \right) \left(1 - e^{(-t^* R_0 B_0)} \right) + e^{(x_0 - t^* B_0)} \right) \tag{32}$$

Hence, if U_0 and B_0 are chosen so that the velocity never vanishes, the solution for the scalar field is:

$$\phi(t, x) = \mathcal{H}(x^*(t^*) - x_0), \tag{33}$$

where the position of the discontinuity $x^*(t^*)$ is given by relation (32).

On figure 29, the solution described above is plotted at time $t = 0.2$ with the parameters: $x_0 = 0.3$, $U_0 = 2$, $R_0 = 2$ and $B_0 = -1$. It can be noted that these choices lead to a non-negative velocity.

6.3 A class of analytical solutions for the convection problem in non-conservative form

We focus here on a class of analytical solutions for system (37). The solution proposed here is based on the results of previous section 6.2. Since the mass equation (i.e. the first equation) of (37) is the same than that of system (2), the density (27) and the velocity (28) functions proposed in section 6.2 are also solutions for system
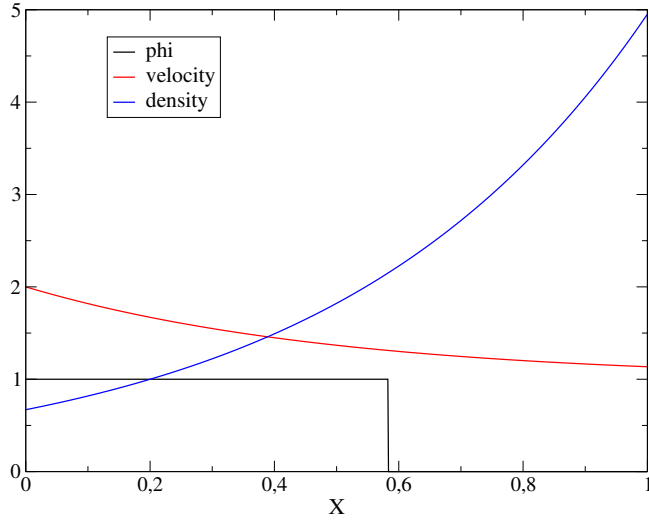
Figure 29: Solution at time $t = 0.2$ for the parameters $x_0 = 0.3$, $U_0 = 2$, $R_0 = 2$ and $B_0 = -1$.

(37). The only difference is that the initial discontinuity for ϕ is now advected with the convection field $a(\rho, U)$, and provided that $a(\rho, U)$ does not depend on time, equation (31) becomes:

$$t^* = \int_{x_0}^{x^*} \frac{dx}{a(\rho, U)}. \tag{34}$$

Equation (34) gives the abscissa x^* of the discontinuity of ϕ at time t^*, when the initial discontinuity is located at x_0 at time $t = 0$. We choose now a specific form for $a(\rho, U)$:

$$a(\rho, U) = \frac{\rho(t = 0, x)U(x)}{\rho(t = 0, x = 0)},$$

where ρ and U are respectively given by (27) and (28). Using the latter relations, we find that:

$$a(\rho, U) = U_0 + B_0 \left(1 - e^{(-R_0 x)}\right), \tag{35}$$

and thus $a(\rho, U)$ does not depend on time. As in section 6.2, equation (34) with the choice (35) can be integrated and it yields:

$$x^* = \frac{1}{R_0} \ln (U_0 + B_0) - \frac{1}{R_0} \ln \left(B_0 - \left(B_0 - (U_0 + B_0)e^{(-R_0 x_0)}\right) e^{(-R_0(U_0 + B_0)t^*)}\right) \tag{36}$$

On figure 30, the solution described above is plotted at time $t = 0.15$ with the parameters: $x_0 = 0.3$, $U_0 = 2$, $R_0 = 1$ and $B_0 = -1$. It can be noted that these choices lead to a non-negative velocity.

6.4 Application to a non-conservative advection problem

Some problems of transport of sharp fronts are associated with an advection field which is different from the velocity field U of the flow. The application of the GRU step is studied here in a non-conservative framework. We thus consider now the system of equations:

$$\begin{cases} \partial_t (\rho) + \partial_x (\rho U) = 0, \\ \partial_t (\phi) + a(\rho, U) \, \partial_x (\phi) = 0, \end{cases} \tag{37}$$

As for system (2), this system of equations involves a density ρ and a velocity field U. In the following, a class of analytical solutions is proposed in appendix 6.3 on the basis of the class of solutions proposed in appendix 6.2 for system (2). In system (37), the scalar quantity ϕ is advected with the speed $a(\rho, U)$. We assume that U is a smooth field and that $(a : \mathbb{R}^+ \times \mathbb{R} \to \mathbb{R})$ is a smooth function. We focus now on a two-step scheme that is based: first on the Lax-Friedrichs numerical scheme recalled below, and then on the GRU step.

In order to compute numerical approximations of ϕ, we use the classical Lax–Friedrichs scheme adapted to a non-conservative framework. Considering a sequence $(\phi_k^n)_{k \in 1, N_c}$ at time t^n, we have:

$$\phi_i^{n+1,*} = \phi_i^n - \frac{a(\rho_i^n, U_i^n)\Delta t}{2\Delta x}(\phi_{i+1}^n - \phi_i^n) + \frac{r^n \Delta t}{2\Delta x}(\phi_{i+1}^n - 2\phi_i^n + \phi_{i-1}^n), \tag{38}$$
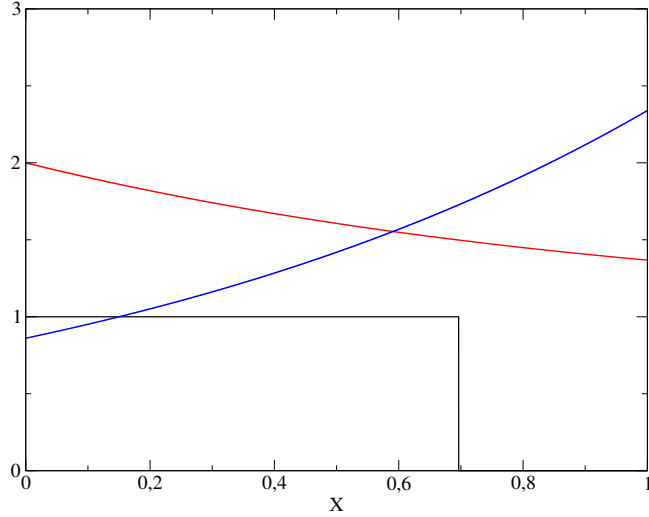
Figure 30: Solution at time $t = 0.15$ for the parameters $x_0 = 0.3$, $U_0 = 2$, $R_0 = 1$ and $B_0 = -1$.

with $r^n = \max_{k \in 1, N_c} (a(\rho_k^n, U_k^n))$. The time step is chosen such that $\Delta t = \Delta x/(2r^n)$. This scheme is an explicit, first order scheme and it is TVD.

Two test cases are investigated here using the Lax-Friedrichs scheme described above and the GRU step introduced in section 2.2. For the first test case, we consider that $a(\rho, U) = U$ and we use the analytical solution that was already used in section 2.4. The second test case involves the analytical solution proposed in section 6.3 for $a(\rho, U) = \frac{\rho(t=0,x)U(x)}{\rho(t=0,x=0)}$, where the variables ρ and U are those proposed in section 6.2. Convergence curves are then built for meshes with 50 to 150000 cells, following the same procedure than that described in section 2 devoted to the conservative framework, see figure 31. It can clearly be observed that the Lax-Friedrichs scheme has a convergence rate of $1/2$ without the GRU step, whereas with the GRU step the convergence rate is equal to 0.85. Moreover, the GRU step improves significantly the accuracy on coarse meshes. We then recover the same behavior than in section 2.

6.5   Computing the Halton-Van der Corput sequence

In the numerical tests the random number ω^n introduced in the GRU step has been replaced by using (K_1, K_2) Halton-Van der Corput sequences. These are low discrepancy sequences on $[0, 1]$. The parameters of the sequence, K_1 and K_2, are two integers relatively prime and such that $K_1 > K_2 > 0$. The nth element, ω^n, of the sequence is computed using the following algorithm [21]:

$$\omega^n = \sum_{i=0}^{m} A_i K_1^{-(i+1)},$$

with,

$$A_i = rem(K_2 a_i, K_1) \qquad \text{and} \qquad n = \sum_{i=0}^{m} a_i K_1^i,$$

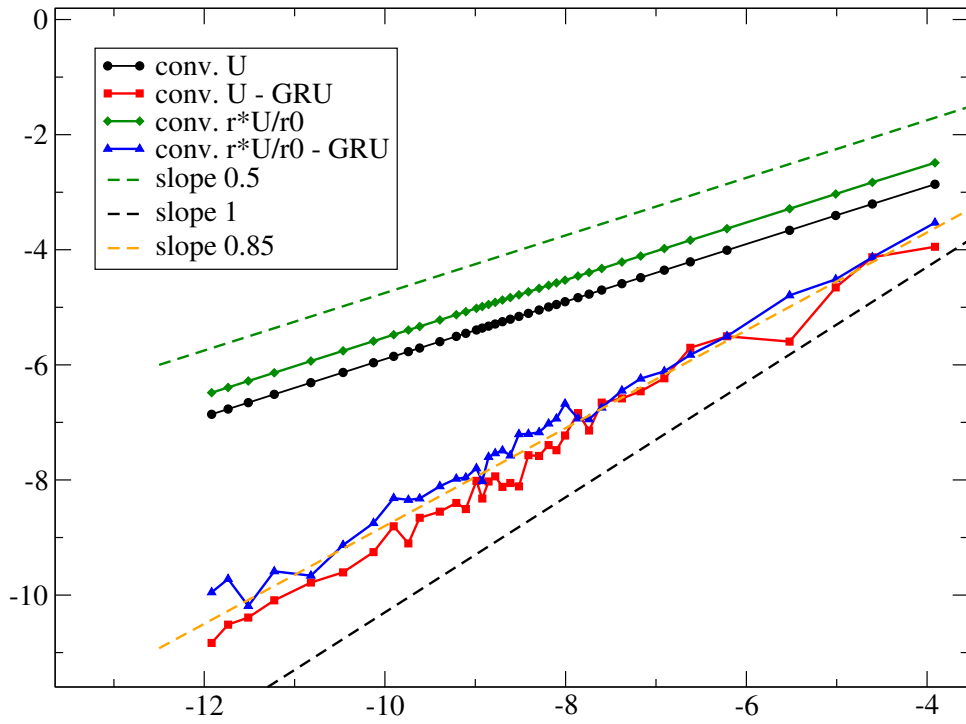and where $rem(a, b)$ is the remainder of the division of a by b.

Figure 31: Convergence curves for the non-conservative advection problem. The black and green curves correspond to the Lax-Firedrichs scheme without the GRU step, whereas for the blue and red curves the GRU step has been accounted for. The case $a = U$ corresponds to the black and red curves. The case $a(\rho, U) = \frac{\rho(t=0,x)U(x)}{\rho(t=0,x=0)}$ corresponds to the green and blue curves. The meshes contain from 50 to 150000 cells.

References

[1] F. BETANCOURT, R. BÜRGER, C. CHALONS, S. DIEHL, AND S. FARÅS, *A random sampling method for a family of temple-class systems of conservation laws*, Numerische Mathematik, 138 (2018), pp. 37–73.

[2] R. BÜRGER, C. CHALONS, AND L. M. VILLADA, *Antidiffusive and random-sampling lagrangian-remap schemes for the multiclass lighthill–whitham–richards traffic model*, SIAM Journal on Scientific Computing, 35 (2013), pp. B1341–B1368.

[3] A. J. CHORIN, *Random choice solution of hyperbolic systems*, Journal of Computational Physics, 22 (1976), pp. 517–533.

[4] P. COLELLA, *Analysis of the effect of operator splitting and of the sampling procedure on the accuracy of glimm's method*, Report No. LBL-8774. California Univ., Berkeley (USA). Lawrence Berkeley Lab., (1978).

[5] ——, *Glimm's method for gas dynamics*, SIAM Journal on Scientific and Statistical Computing, 3 (1982), pp. 76–110.

[6] F. COQUEL, S. JIN, J.-G. LIU, AND L. WANG, *Entropic sub-cell shock capturing schemes via jin-xin relaxation and glimm front sampling for scalar conservation laws*, Mathematics of Computation, 87 (2018), pp. 1083–1126.

[7] F. DELARUE AND F. LAGOUTIÈRE, *Probabilistic analysis of the upwind scheme for transport equations*, Archive for rational mechanics and analysis, 199 (2011), pp. 229–268.

[8] B. DESPRÉS, *Finite volume transport schemes*, Numerische Mathematik, 108 (2008), pp. 529–556.

[9] B. DESPRÉS, S. KOKH, AND F. LAGOUTIÈRE, *Sharpening methods for finite volume schemes*, Handbook of Numerical Analysis, 17 (2016), pp. 77–102.

[10] T. GALLOUËT, J.-M. HÉRARD, AND N. SEGUIN, *A hybrid scheme to compute contact discontinuities in one-dimensional euler systems*, ESAIM: Mathematical Modelling and Numerical Analysis, 36 (2002), pp. 1133–1159.

[11] T. GALLOUËT, J.-M. HÉRARD, AND N. SEGUIN, *Some recent finite volume schemes to compute euler equations using real gas eos*, International journal for numerical methods in fluids, 39 (2002), pp. 1073–1138.

[12] ——, *On the use of symmetrizing variables for vacuums*, Calcolo, 40 (2003), pp. 163–194.

[13] J. GLIMM, *Solutions in the large for nonlinear hyperbolic systems of equations*, Communications on pure and applied mathematics, 18 (1965), pp. 697–715.

[14] A. HARTEN AND P. D. LAX, *A random choice finite difference scheme for hyperbolic conservation laws*, SIAM Journal on Numerical Analysis, 18 (1981), pp. 289–315.

[15] A. HARTEN, P. D. LAX, AND B. V. LEER, *On upstream differencing and godunov-type schemes for hyperbolic conservation laws*, SIAM review, 25 (1983), pp. 35–61.

[16] P. HELLUY AND J. JUNG, *Interpolated pressure laws in two-fluid simulations and hyperbolicity*, Finite Volumes for Complex Applications VII-Methods and Theoretical Aspects, (2014), pp. 37–53.

[17] J. JUNG, *Numerical simulations of two-fluid flow on multicores accelerator*, phd thesis, Université de Strasbourg, https://tel.archives-ouvertes.fr/tel-00876159, Oct. 2013.

[18] D. SERRE, *Systems of Conservation Laws 1: Hyperbolicity, entropies, shock waves*, Cambridge University Press, 1999.

[19] D. SHE, R. KAUFMAN, H. LIM, J. MELVIN, A. HSU, AND J. GLIMM, *Front-tracking methods*, Handbook of Numerical Analysis, 17 (2016), pp. 383–402.

[20] J. SMOLLER, *Shock waves and reaction—diffusion equations*, vol. 258, Springer Science & Business Media, 2012.

[21] F. TORO ELEUTERIO, *Riemann Solvers and Numerical Methods for Fluid Dynamics: A Practical Introduction*, Springer, Berlin, (1997).

[22] S. T. ZALESAK, *Fully multidimensional flux-corrected transport algorithms for fluids*, Journal of computational physics, 31 (1979), pp. 335–362.